CFD analysis on hydrogen production from methane pyrolysis by solar energy

Matiowos Tecle

University of Bergen, Department of Physics and Technology

Bergen, Norway

May 31, 2021

A thesis in partial fulfillment of the requirements for the degree of *Master of Science* in the subject of process technology; multiphase system

Preface

My thesis is the part of the course PRO399. This course is the final part of the master's program in process technology at the University of Bergen. The project in this thesis was given by the University of Bergen from the Department of Physics and Technology, which was performed in the period of 15.08.2020 - 01.06.2021.

This task has been very exciting and challenging, which makes me achieve and dig in more knowledge.

I want to thank my supervisor professor Pawel Kosinski from the Department of Physics and Technology at the University of Bergen. I am very grateful for the time he spent and for his valuable contributions throughout the project period.

Bergen, 01. June. 2021

Matiowos Tecle

Abstract

Methane pyrolysis by solar energy is one of the methods to produce hydrogen without greenhouse gas emissions like CO_2. The final products in methane pyrolysis from solar energy are hydrogen and carbon solid, and this has been studied experimentally by different researchers. In some cases, it is challenging to analyze and study in high-temperature areas experimentally due to the limitation of instruments. Computational fluid dynamics (CFD) is a method to get an understanding of the flow, where experimental access is not possible.

The objective of this thesis was to perform CFD analysis on one of the methods to produce hydrogen from methane pyrolysis by solar energy. It was a vortex flow solar reactor method that was chosen for this CFD analysis. This was done experimentally by other researchers. The CFD analysis in this thesis was to study the temperature distribution, the characteristic of the flow, the distribution of gases, and soot or carbon formation in the reactor.

The STAR-CCM+ simulation tool was used for this CFD analysis. The simulation results showed that the temperature of the reactor increased with time as expected after heating to the one side of the reactor, which was assumed to be a glass window. The final products were mainly hydrogen and soot particles after reaching a high temperature above 1300 K. The $k - \epsilon$ model was chosen to compute the turbulent flow and the effect of swirl flow. The geometry of the vortex flow solar reactor was designed in two ways, where the methane inlet was placed at the rear and at the front of the reactor. The outlet temperature with methane inlet at the rear was detected higher than for the case where the inlet was at the front.

The absorption coefficient was also varied to investigate the temperature of the reactor. It was detected that the outlet temperature of the reactor increased with the increasing of the absorption coefficient. From this CFD analysis, it was observed that the soot or carbon particles formation was related to the production of C_2H_2, where the production of soot particles increased with the increase of C_2H_2 mass fraction. To model the heat source for the vortex flow solar reactor, the total power that enters the solar reactor was assumed

to be about 5 kW. The heat source was modeled in two ways depending on the condition of solar irradiation or direct normal irradiation (DNI) value. Only the volumetric heat source (W/m^3) was modeled, when it was assumed the concentrated DNI that enters to the solar reactor was enough to reach 5 kW. The combination of volumetric and electric (W/m^2) heat source was modeled, when it was not enough concentrated DNI.

Table of Contents

1 Introduction

Due to human activity, the Earth's climate is changing over time. This is called "anthropogenic climate change". Burning fossil fuels like coal, oil, and natural gas to produce energy are one of the reasons for releasing "greenhouse gases" (GHG) into the atmosphere [3, 5, 26].

The main greenhouse gases are carbon dioxide (CO_2), methane (CH_4) and nitric oxide (NOx). These gases accumulate in the atmosphere and allow radiation from the sun to pass through, but trap some of the heat radiating back from the Earth, and it is called the "greenhouse effect". CO_2 is the most important GHG because most of the GHG-emission is from CO_2. Of the total emissions, CO_2 has a share of about 65 % that came from the use of fossil fuel in 2014. Its annual emissions grew by about 80 % between 1970 and 2004 [3, 5, 26]. The concentrations of GHG like CO_2 has also been increasing in 2019 and 2020 [39].

The increase of GHG over time results in "global warming" an increase in the Earth's average temperature. Global warming is one of the reasons for climate change that can result in droughts, storms, floods, heatwaves, and others [3, 5, 26]. To reduce GHG emissions, hydrogen appears as one of the most sustainable energy carriers [12].

1.1 Hydrogen production

Hydrogen is one of the energy carriers that can use to produce electricity without realising CO_2. Some of the hydrogen production methods were mentioned in this thesis.

1.1.1 Hydrogen production by reforming

Hydrogen can be made by methane steam reforming (SMR), partial oxidation (POX), and autothermal reforming (ATR). Hydrogen can be produced from natural gas by using steam methane reforming, where water steam and methane converts into hydrogen and carbon monoxide. This reaction is endothermic. After the reforming process, the syngas undergoes a water gas shift. In this water gas shift reaction, carbon monoxide reacts with water to produce additional hydrogen as well as carbon dioxide. This is reaction occurs

with the help of the catalyst. The SMR-method is the most and widely used to make hydrogen [20].

In the POX process, hydrogen can be made from natural gas by using a limited oxygen supply that reacts with any hydrocarbons. The products are hydrogen and carbon monoxide in this process. This reaction is exothermic, in contrast to the highly endothermic SMR reaction. After the water gas shift reaction then additional hydrogen and carbon dioxide are produced [20]. In the ATR process, the POX and SMR combines in one reactor. The natural gas is partially oxidized in a combustion zone, while steam is injected in an SMR zone. The final products are hydrogen and carbon dioxide [8]. After the water gas shift reaction, The hydrogen and carbon dioxide are produced as additional.

Those methods can produce hydrogen but they have common disadvantages. The disadvantage of SMR, POX, and ATR methods is the direct carbon-emission due to the production of CO_2. It results in significant costs to capture and store CO_2 [25].

1.1.2 Hydrogen production by in-situ gasification

In-situ gasification is one of the modern methods that has been tested in Canada to produce hydrogen from bitumen [19]. In this process, water vapor and oxygen are pumped over fires deep in the oil well. Special membranes release only hydrogen, while carbon dioxide remains underground. One of the challenges of this process is that it is associated the difficulty of injectant conformance and control, hydrogen transport to production wells, and hydrogen separation from the product gases.

1.1.3 Hydrogen production by thermal/pyrolysis of methane cracking

To avoid CO_2-emissions, thermal decomposition of methane gas by solar energy into hydrogen gas and carbon solid in the absence of catalyst has been studied using different methods by different researchers. The overall reaction can be written as [28]:

$$CH_4 \longrightarrow 2\,H_2 + C \tag{1}$$

This reaction is an endothermic reaction that demands heat to react. The main advantages of this method is hydrogen produced without CO_2 emission and the carbon

is produced in solid form, which makes it easier to capture. One of the methods was worked out by Rodat et al. [28]. The work was based on the concept of indirect heating from solar irradiation. Their research was performed in a medium-scale solar reactor of 10 kW. The solar reactor was composed of a cubic cavity receiver, see Figure 1. The concentrated solar irradiation was entered through a quartz window via a 9 cm-diameter aperture. The reacting gas was injected inside four graphite tubular reaction zones that were settled vertically inside the cavity. This was indirect heating because methane gas was heated by the hot wall of the four tubes. The tubes absorbed heat from solar irradiation that entered to the reactor and the cavity. The gas mixture of argon and methane was introduced in each tube with controlled composition. The reactor was designed for a nominal power of 10 kW and placed at the focus of the 1 MW solar furnace of the laboratory. The furnace was composed of a field of 63 heliostats (45 m^2 per heliostat) and one parabolic concentrator. The parabolic concentrator (1830 m^2) delivered up to 9000 suns or 9000000 W/m^2 at the focal plane, see Figure 1 [28].

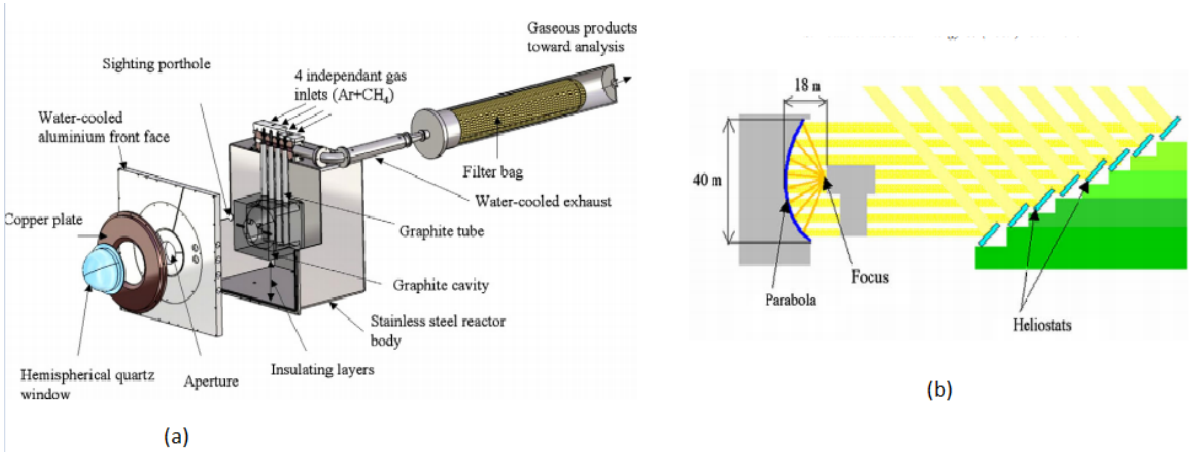

Figure 1: A schematic of solar reactor and solar concentrator, where (a) is the 10 kW solar reactor and (b) is the scheme of solar furnace [27, 28].

Methane and hydrogen yield of up to 98 % and 90 %, respectively were achieved at 1770 K from this experimental work. It was also observed that hydrogen production increased with the increasing temperature of the solar reactor. The hydrogen produced was 42 % at 1670 K and 63 % at 1740 K. Small amounts of the products like C_2H_2, C_2H_4, and C_2H_6 was also seen during this experimental work. The production of C_2H_2 was higher

than C_2H_4 and C_2H_6, with a mole fraction of about 5 %. This experimental work was also compared in 3D simulation, where the temperature was increased with time up to 2160 K in the reactor.

A small-scale 1 kW solar reactor for methane decomposition by direct heating was also investigated by Abanades and Flamant [1, 2]. The reactor consisted of a tubular graphite receiver, in which a mixture of Ar and CH_4 flows, as shown in Figure 2. Methane gas absorbed heat directly from solar radiation [1, 2].

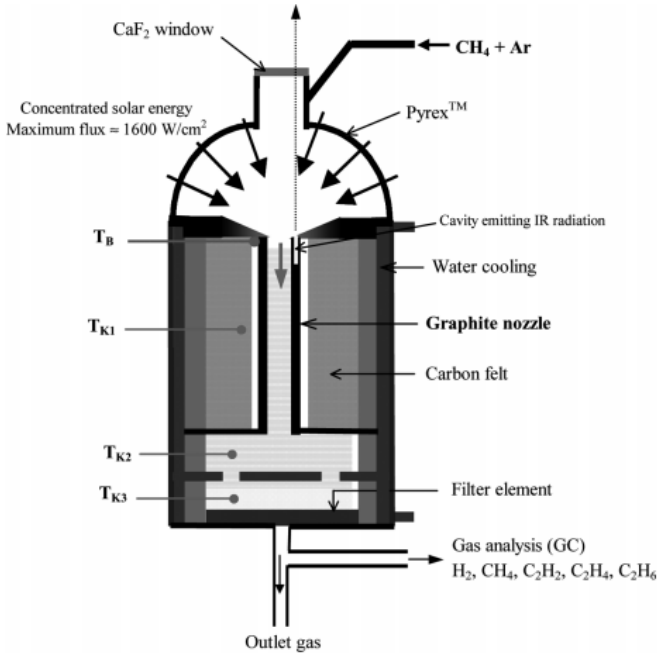

Figure 2: Schematic of 1 kW solar reactor [1, 2].

The gas was also heated mainly by conductive and convective heat transfer from the hot wall. Argon gas was injected at the top of the window to prevent the window from particle clogging that can cause breakage and transport carbon particles by the reaction out of the reactor [1]. From Abanades and Flamant's experimental work, the yield of H_2 was 90 %. Carbon particles that were formed during the reaction can also be directly heated because they serve as radiant absorbers. The production of H_2 increased from 12 % to 65 % when the temperature increased from 1563 K to 1813 K, and the mole fraction of C_2H_2 was also increased from 0.2 % to 2%.

CFD analysis was also carried out by Abanades and Flamant, where a 2D axisymmet-

ric model was chosen to predict fluid flow characteristics, temperature distribution, CH_4 and H_2 concentration profiles, and conversion rate. From their CFD analysis, the temperature was increased with time and the highest temperature area was at the graphite wall. According to the analysis, the reaction occurred in the higher temperature areas of the reactor. The production of H_2 and the conversion rate of CH_4 increased with the increasing temperature [1, 2].

A vortex flow solar reactor of 5 kW was also researched by Hirsch and Steinfeld, and is shown in Figure 3 [15, 23].

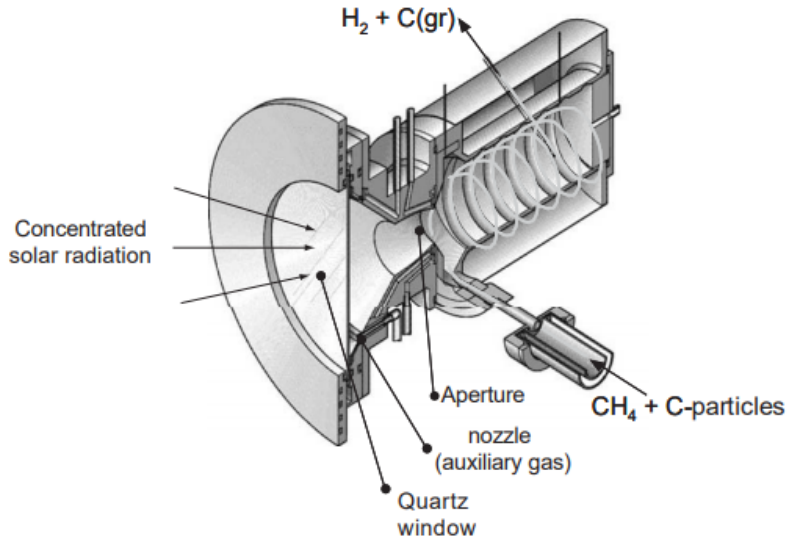

Figure 3: A scheme of a vortex flow solar reactor [15].

As shown in Figure 3, a vortex flow of CH_4 injected into a cavity-receiver with carbon particles that serve simultaneously as radiant absorbs and nucleation sites for the heterogeneous decomposition reaction. Similarly to Abanades and Flamant experimental set-up, Ar was injected at the wall near the window of the reactor. The mixture of CH4, C-particles, and Ar was injected tangentially to make the vortex flow. The tube or cylinder of this solar reactor was made of different materials like steel alloy that overlapping with 96 % AlO_3 and 4 % SiO_2 ceramic thermal insulation to minimize conduction heat loss [15].

In their work, the thermal decomposition of methane was investigated, at the temperature

with a range of 1300-1600 K in the reactor. The maximum methane conversion was about 98 % and a hydrogen yield of 99.1 % was achieved [23]. The outlet and reactor temperature was necessary to reach up to 1300 - 1600 K to crack methane and gives hydrogen as a product [15].

In Hirsch and Steinfeld's work, the inlet port of methane and carbon particles was analyzed in different configurations. The reactor was mounted horizontally in configuration 1 and 3, and it was mounted vertically in configuration 2. Configuration 1 was when the inlet port of methane and carbon particles placed at the rear side of the reactor, where the outlet port was at the front. The inlet port was placed at the rear of the reactor in configuration 2. In the configuration 3, the inlet port of methane and carbon particles placed at the front side of the reactor, where the outlet port was at the rear. The outlet and reactor temperature was increased with time in both ways of methane and carbon particles inlet. [15]. The maximum outlet temperature for the configurations 1, 2 and 3 were 1018, 985, and 1197 K, respectively.

The experimental work of the vortex flow solar reactor by Hirsch and Steinfeld was also analyzed in CFD simulation using Fluent software by Ozalp et al. [23]. In their CFD analysis, the distribution of temperature and mass fraction of argon, methane, and hydrogen was investigated. Their reactor was designed with and without carving form for CFD analysis. The carving helped to make vortex/swirly flow in the reactor. The formation of eddies was higher for the case when the solar reactor was designed with a carving. This also led a higher outlet temperature than without carving tube of the solar reactor. It was also observed that argon prevented the window by pushing methane gas away from the window and the reaction occurred at the middle of the reactor, where the temperature was high [23].

The common concept of those three methods that were mentioned above were producing hydrogen without CO_2 emission. Carbon particles were also produced with hydrogen. The formation of carbon particles in the reaction has a relation with the production of C_2H_2. The carbon or soot formation from C_2H_2 and C_2H_4 pyrolysis at different temperatures was studied experimentally by Ruiz et al. [30]. In Ruiz et al. paper, C_2H_2 and C_2H_4 gas diluted in nitrogen were fed into the reaction system or reactor and was heated at

different temperatures from 1273 K to 1473 K. It was observed that the soot formation increased with the increase of C_2H_2 and C_2H_4. It was also observed that the soot or carbon particle formation increased with the increase in temperature. The diameter of those carbon products was in the range of 10-50 nm. A similar range of carbon particle size was also obtained the other, aforementioned methods.

1.2 The objective of this thesis

The goal or objective of this thesis was computational fluid dynamics (CFD) analysis using STAR-CCM+ software on one of hydrogen production methods from methane pyrolysis by solar energy.

The method that was chosen for the CFD research was to inject methane gas into a glass tube, and heat it by sun radiation. Since it is not always enough sun radiation or direct normal irradiation (DNI) to heat the reactor, it was also assumed that additional heat was provided by electricity. This method was analyzed experimentally by Rodat et al, where the tubes was made of graphite and only heated by solar energy. A hybrid or solar-electric reactor was tested for thermal chemical processing by Rowe et al. [29]. This hybrid solar reactor was the same as Rodat et al.'s reactor but it includes six molydisilicide heating elements capable of supplying electrical heating at temperatures up to 1700 K [29].

Solar irradiance is the measure of how much is the amount of sunlight energy or radiation is hitting a square meter of each second. The unit of solar irradiation is often given in W/m^2. DNI is the same as solar irradiance but it measured at the surface of the Earth at a given location with a surface element perpendicular to the sun. DNI-value is necessary for instruments like solar reactors and concentrators [6].

The value of DNI is usually not high in northern countries like Norway. In Norway, the highest and lowest DNI value can reach about 0.2 kW/m^2 and 0.1 kW/m^2 respectively in summer and wintertime [32]. Since, about 91 % of electricity is produced from hydropower in Norway [33], Norway's DNI-value was taken into account for the CFD analysis in this thesis.

Methane absorbs solar radiation in the infrared range. Methane molecules can vibrate

but they do not crack in the infrared range as mentioned in section (2.7.2). Thus, it is not enough to heat and crack methane gas by solar radiation using only glass tube. To intensify methane heating, some sides of the tube have to be in other materials than glass. Therefore, the vortex flow solar reactor that was studied experimentally by Hirsch and Steinfeld was more suitable for CFD analysis with the idea of the glass tube. At one of the sides of the vortex flow solar reactor there was a quartz window made of glass. This permitted that permitted sun radiation to enter directly into the tube.

It is not straightforward to implement measuring equipment in a high-temperature reactors [23]. The CFD analysis is therefore needed to observe the character of the fluid flow and compare with some of the experimental results.

The objective of the CFD analysis in this thesis was to study;

- The temperature distribution in the reactor tube.
- Mass fraction distribution of methane, hydrogen, and the main products of the reaction.
- The effect of inlet injection method on swirl/vortex flow.
- Comparing between front and rear inlet.
- Soot formation.

2 Theory

In this section, the main concepts that have been used to analyze the objective of this thesis are mentioned and explained shortly.

2.1 STAR-CCM+

Simcenter STAR-CCM+ is software on computational fluid dynamics (CFD) based simulation that allows to model and analyzes a range of engineering problems involving fluid flow, heat transfer, stress, particle flow electromagnetics, reacting flow, and other related processes [34].

2.2 Fundamental equations

In Simcenter STAR-CCM+ the mathematical models that describe the physics of continua are derived from fundamental laws that express conservation principles. The conservation laws for the continuous fluid are expressed using the Eulerian approach method, that is in a given control volume representing a portion of fixed space where material can flow through. In the following, the basic fundamental equations are discussed [18, 35].

2.2.1 Conservation of mass

The law of conservation of mass or the in fluid dynamics states that the mass flow rate that enters the system or the control volume is equal to the mass flow rate that leaves the control volume plus the accumulation of mass flow rate within the control volume [18, 35].
The differential form of the equation is:

$$\frac{\partial \rho}{\partial t} + \nabla \cdot (\rho \mathbf{V}) = 0\,, \tag{2}$$

where t is time, ρ is density, $\mathbf{V}$ is the flow velocity vector field, thus $\mathbf{V} = (u, v, w)$ components in (x, y, z) direction respectively, and ∇ is a vector operator, it defined as $(\mathbf{i}\frac{\partial}{\partial x} + \mathbf{j}\frac{\partial}{\partial y} + \mathbf{k}\frac{\partial}{\partial z})$.

2.2.2 Conservation of momentum

The conservation of momentum is based on Newton's second law. It says that the net force that acts on the fluid element is equal to its mass times the acceleration of the element or portion of the fluid. For simplicity, it is considered only in the x-direction and it is expressed as: [18, 35],

$$\mathrm{F_x} = \mathrm{ma_x}\,, \tag{3}$$

where $\mathrm{F_x}$ is the net force acting on the fluid element on the x-direction, a_x is the acceleration of the fluid element in x-direction, and m is the mass of the fluid element.
There are two main sources of forces acting on the fluid element. These are:

1. The body forces that act directly on the mass of the fluid element. Examples like gravitational force and centrifugal force. The force is a volumetric mass.
2. Surface forces that act on the surface of the fluid element, due to two sources:
   (a) The shear and normal stress distributions acting on the surface.
   (b) The pressure distribution acting on the surface, that are affected by the outside fluid surrounding the fluid element.

The general equation of conservation of momentum and also known as Navier-Stokes equation is expressed as:

$$\frac{\partial(\rho u)}{\partial t} + \nabla \cdot (\rho u \mathbf{V}) = -\frac{\partial p}{\partial x} + \frac{\partial(\tau_{xx})}{\partial x} + \frac{\partial(\tau_{yx})}{\partial y} + \frac{\partial(\tau_{zx})}{\partial z} + \rho f_x\,. \tag{4}$$

The left-hand side of the equation (4) represents the volumetric mass and acceleration and the right-hand side represents the pressure distribution, stress forces, and body force, respectively.

2.2.3 Conservation of energy

The conservation of energy is based on the first law of thermodynamics that states energy is conserved. This means that energy cannot be created or destroyed but can transform from one form to another [18, 35].

The general equation of conservation of energy is expressed as:

$$\frac{\partial(\rho E)}{\partial t} + \nabla \cdot (\rho E \mathbf{V}) = \mathbf{V} \cdot \boldsymbol{f_b} + \nabla \cdot (\mathbf{V} \cdot \boldsymbol{\sigma}) - \nabla \cdot \mathbf{q} + S_E \,. \tag{5}$$

The left-hand side of the equation (5) represent the total rate of change inside fluid, i.e internal and kinetic energy, where E is the total energy per unit mass. The right-hand side represents the net flux heat into element and the rate of work done on element due to body and surface forces, where $\boldsymbol{f_b}$ is body forces per unit volume acting on the fluid, $\boldsymbol{\sigma}$ is stress tensor as the sum of shear and normal stresses, $\mathbf{q}$ is the heat flux for (x, y, z) directions and S_E is the volumetric heat source.

2.3 Mesh/Discretization and judging convergence

A discretizeation is to break the continuous domain into smaller pieces, where the equations are solved. Some of the discretization methods are the finite difference method (FDM), finite element method (FEM), and finite volume method (FVM) [18].

Meshing is a process to represent a geometric domain in a discretized way. Simcenter STAR-CCM+ uses discretization methods to convert the continuous system of equations to a set of discrete algebraic equations, which can be solved using numerical techniques. STAR-CCM+ uses either finite volume or finite element method depending on the mathematical model to discretize the equations. STAR CCM+ uses the FEM in solid mechanics, electromagnetism, and viscous or non-newtonian flow [35].

In the FVM, the solution domain is subdivided into a finite number of small control volumes, that correspond to the cells of a computational grid [35].
In FVM, the integration of the conservation equations is applied to each control volume. Figure 4 shows an example of one cell or control volume that equations are going to apply.

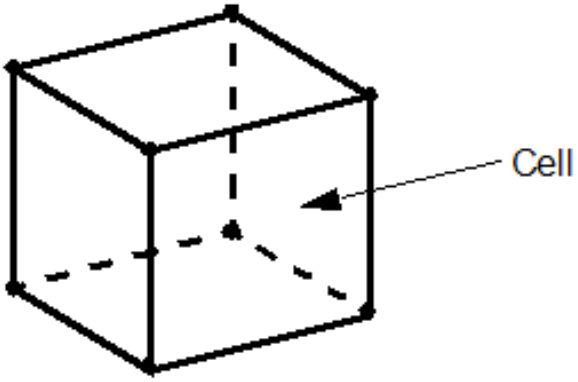

Figure 4: Example of a control volume [36].

The integral form of the conservation of mass is expressed as: [18].

$$\frac{\partial}{\partial t}\iiint_V \rho \, dV + \iint_S \rho \mathbf{V} \cdot \mathbf{dS} = 0 \,. \tag{6}$$

The first term is the time rate of increase of mass inside the volume, V and the second term is the net mass flow out of the entire control volume through the control surface S. The vector elemental surface area is $\mathbf{dS}$.

Poor mesh quality is one of the reasons to reduce the accuracy and efficiency of the solution obtained. Finer mesh size gives better information and accuracy of the domain than the coarser mesh size, but it requires a lot of computational time [35].
STAR-CCM+ provides methods to check mesh quality. Cell quality and skewness angle are some of the methods.

Cell quality is a function of relative geometric distribution of the cell centroids of the face neighbor cells. A cell with a quality of 1.0 is considered as a quality. A cell quality less than 10^{-5} is invalid. Cell skewness angle is designed to measure whether the cells on either side of a face are formed in such a way as to permit diffusion of quantities without these quantities becoming unbounded. Cells with a skewness angle greater than 85^o are considered poor quality cells [35].

Observing residuals, heat, and mass balance is one of the methods to judge whether the solution is going to be converged or not. Generally, when residuals or errors of species

shown below 1, then it is a good sign for converging solution. Heat and mass balance has to be close to 0 if the solution is converging [18, 35].

2.4 Turbulence

Turbulence is described as the random or chaotic motion of fluid flows. The random movement of the fluid is governed by the Navier-Stokes equation. The flow consists of different scale sizes of eddies.
The larger eddies extract energy from the mean flow and transfer their kinetic energy to the smaller eddies, and the smaller eddies transform into thermal energy by viscous or stress forces. Diffusivity, change of momentum, and heat transfer increase in a turbulent flow. Figure 5 shows examples of eddies with their length scale size [11].

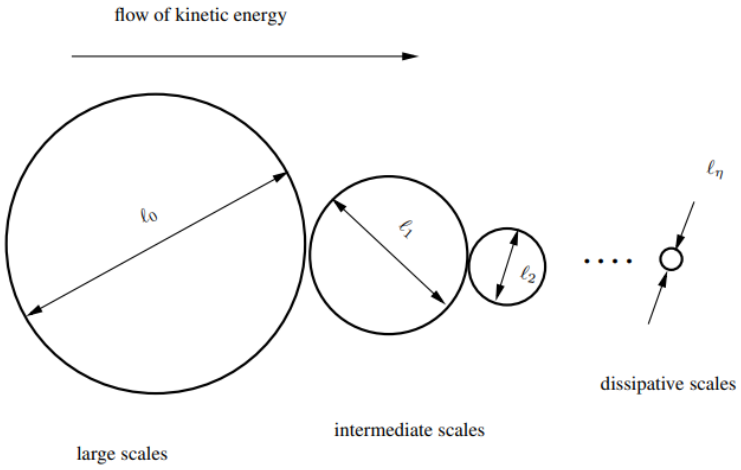

Figure 5: A scheme of eddies in a turbulent flow [11].

In turbulent flow, velocities and other parameters like the pressure have fluctuations because of the chaotic movement of the flow. To capture and resolving of all the fluctuations takes an excessive computational cost. To reduce costs, it is taken an average of those fluctuations instead of solving them directly. Reynolds-Average Navier-Stokes (RANS) is one of the turbulence models that is used in STAR-CCM+ [35].

2.4.1 RANS

The idea of RANS is that the equation is Reynolds decomposition, where a quantity of interest is decomposed into its time-averaged and fluctuating quantities. For example as in equation (7) shown, where ϕ represents velocity components, pressure, energy, or species concentration. $\overline{\phi}$ is the average value and ϕ' is the fluctuating component [35]:

$$\phi = \overline{\phi} + \phi' \,. \tag{7}$$

The mean mass transport equation can be written as:

$$\frac{\partial \rho}{\partial t} + \nabla \cdot (\rho \overline{\mathbf{V}}) = 0 \,, \tag{8}$$

where $\overline{\mathbf{V}}$ is mean or average velocity.

2.4.2 K-Epsilon model

The $k - \epsilon$ is one of the models that solve or determine the eddy viscosity.
Eddy viscosity model is used to make it possible to model the Reynolds stress tensor as a function of mean flow quantities, which means it accounts for the transport and dissipation of energy that was neglected as a result of turbulence modeling [35, 37].

The $k-\epsilon$ model is a two-equation method that solves transport equations for the turbulent kinetic energy k and the turbulent dissipation rate ϵ. Turbulence dissipation is the rate at which the turbulence kinetic energy of those smaller eddies are converted into thermal energy. The $k - \epsilon$ models provide a good computational cost and accuracy. They are good for industrial-type applications that contain complex recirculation, with or without heat transfer. Equation (9) and (10) show an example of transport equations for both the kinetic energy k and the turbulent dissipation rate ϵ [11, 35] :

$$\frac{\partial}{\partial t}(\rho k) + \nabla \cdot (\rho k \overline{\mathbf{V}}) = \nabla \cdot \left((\mu + \frac{\mu_t}{\sigma_k}) \nabla k \right) + P_k - \rho(\epsilon - \epsilon_0) + S_k \,, \tag{9}$$

$$\frac{\partial}{\partial t}(\rho \epsilon) + \nabla \cdot (\rho \epsilon \overline{\mathbf{V}}) = \nabla \cdot \left((\mu + \frac{\mu_t}{\sigma_\epsilon}) \nabla \epsilon \right) + \frac{1}{T_\epsilon} C_{\epsilon 1} P_\epsilon - C_{\epsilon 2} f_2 \rho \left(\frac{\epsilon}{T_\epsilon} - \frac{\epsilon_0}{T_0} \right) + S_\epsilon \,, \tag{10}$$

where μ is the dynamic viscosity,μ_t is turbulent eddy viscosity, $(\sigma_k, \sigma_\epsilon, C_{\epsilon 1} C_{\epsilon 2})$ are model coefficients, P are production terms,f_2 is damping functions that resolve the viscous and buffer-layer, and S terms are the user-specified source.

2.5 Reacting flow

STAR-CCM+ can use either reacting species transport or flamelet model to work with the equation of reacting flow. In equation (5) the chemical source term or the heat from the reaction is added in S_E term in the conservation of energy [35].

2.5.1 Models of reacting flow

The conservation equations that include the chemical source term are solved for all species in a mechanism when reacting species transport model is active while in the flamelet model, the reacting flow system is parameterized by a limited number of flamelet variables which describe the thermochemical state in CFD cell [35].

For example in reacting species transport, STAR-CCM+ solves transport equations for the mass fractions of all species that are involved in the chemical reactions. This model includes complex chemistry for simulating flow using detailed mechanisms within a turbulent flame in which kinetic phenomena are significant. In the flamelet model, STAR-CCM+ uses mixture fraction or the atomic mass fraction that originated from the fuel stream as one parameter [35].
The conservation equations for species mass fractions Y_i are expressed in this equation:

$$\frac{\partial \rho Y_i}{\partial t} + \nabla \cdot (\rho U Y_i) = \nabla \cdot (J_i + \frac{\mu_t}{\sigma_t} \nabla Y_i) + S_{Y_i} \,. \tag{11}$$

This equation can be defined from the transport equation, where the first left-hand side represents the time rate of change of species and the second term is the convective flux. From the right-hand side, the first term represents the diffusive flux of the species and the last term S_{Y_i} represents the mass fraction source term from reactions [35].

2.5.2 Reaction rate

The reacting species transport model calculates the reaction rates for all reactions in the chemical mechanism, to solve the source term of the transport equation.

Equation (12) is the Arrhenius equation, that the reaction rate depends on temperature

[35] :

$$k = Ae^{-\frac{E_a}{RT}}\,, \tag{12}$$

where E_a is the activation energy, R is the universal gas constant, A is the frequency factor and k is the rate constant.

2.6 Hydrocarbons

Hydrocarbon is a chemical compound made of hydrogen and carbon atoms. Most of the hydrocarbons occur in nature. Petroleum and natural gas like methane are made of hydrocarbons. Those can use as fuels and lubricants as well as raw materials for the production of plastics, soaps, perfumes, and other industrial chemicals [4, 24].

Hydrocarbons like petroleum formed from organic matter which was deposited underground and remained buried under the absence of free oxygen conditions for millions of years. Over the years the organic matter buried by layers of sand and others. The increase of temperature and pressure slowly transformed the organic matter into hydrocarbons like oil, kerogen, and gas [40].

Hydrocarbons are divided into aliphatic and aromatic compounds. The aliphatic compound is where the carbon atoms connected by single, double, or triple bonds to form a nonaromatic structure, and this group divided into three classes. The classes are alkanes which are the single bond between carbon atoms, alkenes have a double bond, and alkynes have a triple bond [4, 24].

Thermal cracking is one of the processes to break the large hydrocarbons into smaller ones like methane gas by using high temperature. This process is the same as the pyrolysis process if the cracking is with the absence of air or oxygen. In cracking of hydrocarbons by heating or high temperature, the carbon-carbon bonds are broken so that each carbon atom ends up with a single electron or the free radicals are formed as shown in Figure 6 [10, 13].

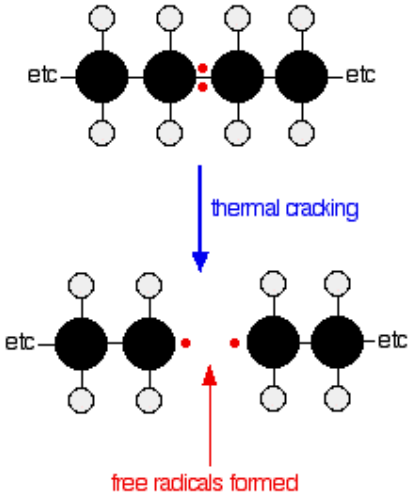

Figure 6: A scheme of thermal or pyrolysis cracking [10].

2.7 Methane gas

Like large or long-chain hydrocarbons can be broken into smaller chains by pyrolysis or breaking with the absence of air or oxygen by using high temperature, methane can also be broken by pyrolysis to produce hydrogen and carbon solid [16].

2.7.1 Reaction mechanism of methane pyrolysis

The reaction mechanism of hydrocarbons like methane is quite complex to understand in detail. The overall reaction of methane cracking at high temperature above 1300 K by free radical mechanism, where the main gas products of methane are hydrogen, ethane, ethene, and ethyne can be expressed as [16] :

$$2\,CH_4 \xrightarrow{H_2^+} C_2H_6 \xrightarrow{H_2^+} C_2H_4 \xrightarrow{H_2^+} C_2H_2 \xrightarrow{H_2^+} 2\,C\,. \tag{13}$$

Carbon is also formed as a solid. If the temperature is high above 1400 K then the final products became hydrogen and carbon solid [16]. Figure 7 shows the network of methane reaction mechanism that occurs under the pyrolysis process. This model is from Billaud et al. [22], where methane pyrolysis was observed in a tubular flow reactor in

the temperature range 1473 - 1773 K at atmospheric pressure and heated by an electric furnace.

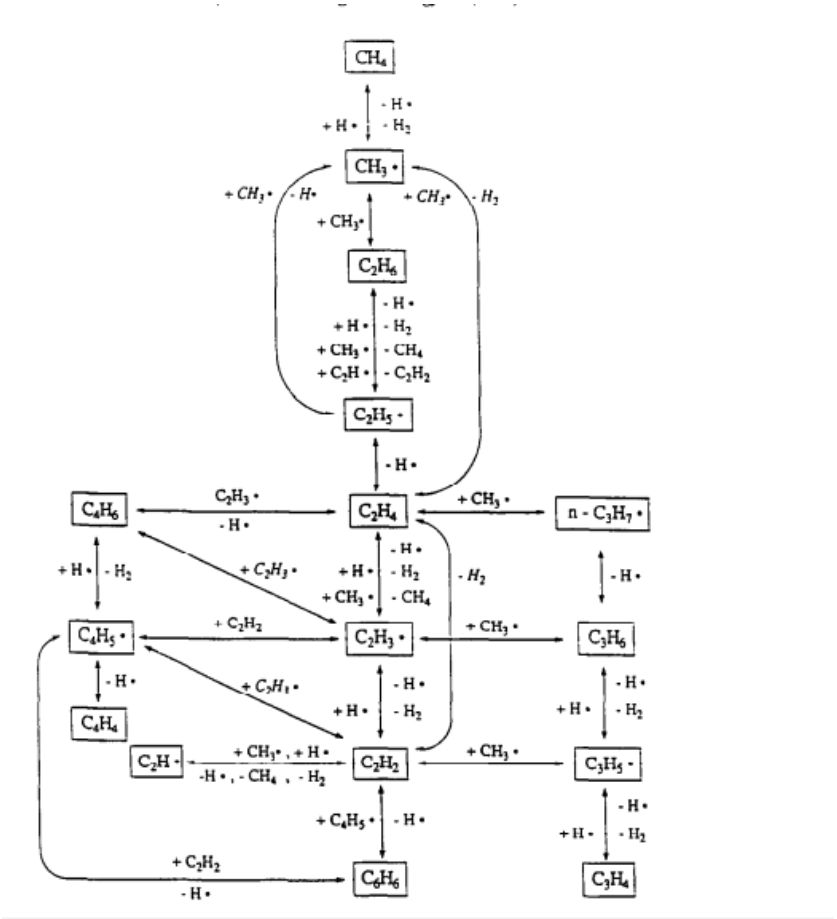

Figure 7: Reaction mechanism of methane by pyrolysis cracking [22]

2.7.2 Methane spectrum

Molecules can absorb radiation for example from sunlight in different processes. The first is when radiation is absorbed and leads to a higher rotational energy level in a rotational transition. The second is when quantized energy is absorbed by the molecules and occurs in vibrational transition. The third one is when electrons of molecules being raised to higher electron energy which is electronic transition [17, 31].

The order of the energy level is: rotational<vibrational<electronic. The rotation of the molecule occurs when the molecules absorb longer wavelengths and this energy is not enough to cause the molecules to vibrate and electron transition. When the molecules absorb infrared then, the molecules have enough energy to vibrate. In order for those

electrons of molecules to go to the transition state, higher energy or ultraviolet (UV) region has to be absorbed. UV light can be enough energy to break the chemical bonds of the molecules. Methane gas is one of the gasses that can absorb infrared region, the energy that can only vibrate. It means that the molecule can stretch and bend [17, 31].

2.8 Beer-Lambert law

The Beer-Lambert law relates the attenuation of light to the medium or properties of the material through which the light is traveling [21]. The concept of Beer-Lambert's law is illustrated in Figure 8.

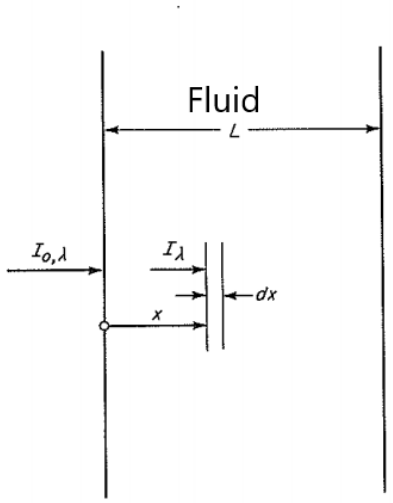

Figure 8: Example of a radiant travel through a fluid [21].

In Figure 8, $I_{0,\lambda}$ is the incoming radiation with specific wavelength, λ. L is the thickness of the medium. x is the distance how far the light travels in the x-coordinate. From this idea shown in Figure 8, the Beer-Lambert equation is expressed as:

$$I_\lambda = I_0 \cdot e^{-k \cdot x} \,. \tag{14}$$

Equation (14) contains an exponential function. The radiation intensity $I_\lambda\,[\mathrm{W/m^2}]$ decreases as it travels along x. k is the absorption coefficient of the fluid and its unit is $\mathrm{m^{-1}}$. The absorption coefficient is defined or determines how far can radiation travel as it

passes through the medium [21, 41]. For example, gases have a low absorption coefficient that means their almost transparent, while solids have a high absorption coefficient [21]. Methane absorption coefficient as a function of wavelength is shown in Figure 9. This figure was from Grundy et al. research [14], where the absorption coefficient of methane was measured in the infrared region in different temperatures.

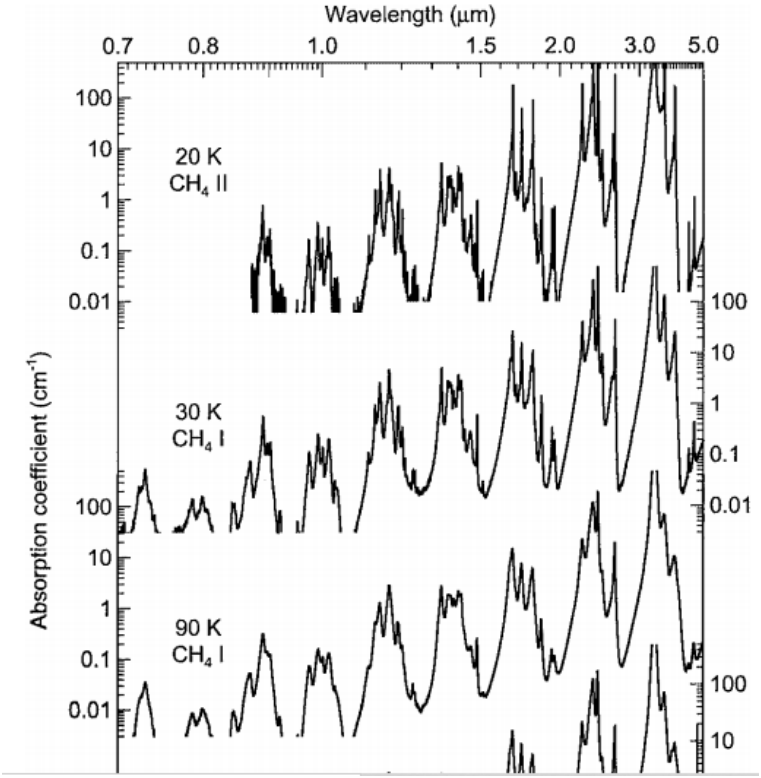

Figure 9: Methane absorption coefficient [14].

The Beer-Lambert equation can be written in a volumetric unit [W/m^3] as the derivative of equation (14):

$$Q_v = -k \cdot I_0 \cdot e^{-k \cdot x}\,, \tag{15}$$

where Q_v is the volumetric heat source.

2.9 Soot

Soot is a black carbonaceous particle which formed or observed during the combustion of hydrocarbons. Soot can be mostly seen or formed in incomplete combustion or pyrolysis

process. For example, a typical engine can emit soot at a rate of 0.2 to 0.6 g/km. Soot or carbon black can be used for the production of automobile tires, in furnaces for industrial application, and also can be used for heat transfer [7, 38].

The mechanism for soot formation is complex and it is not clearly understood but it can be modeled in a general form. The major steps in the mechanism of soot formation are particle nucleation, soot particle coagulation, soot particle surface reactions, and soot particle agglomeration. These steps are shown in Figure 10 [7].

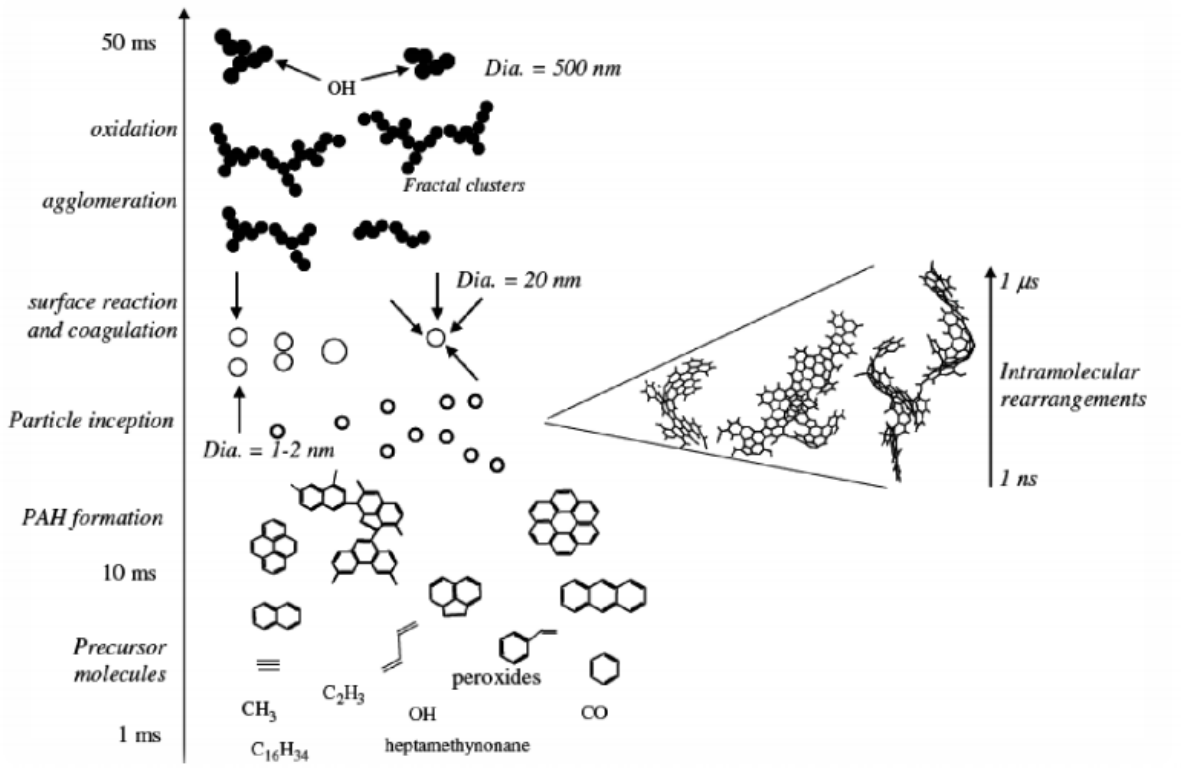

Figure 10: Example of soot formation model [7].

Acetylene C_2H_2 and polycyclic aromatic hydrocarbons (PAH) are the main ones to cause that soot surface growth, in other words, to grow the formation of soot. During the mechanism or process, the C_2H_2 is polymerized to form a ring, or aromatic hydrocarbons like PAH are formed [7].

From PAH, the particle nuclei are produced. Particle nuclei are initiation steps or serve

as nucleation sites for soot formation. Those nucleation sites serve as a bridge for the transition from gaseous hydrocarbons to macro molecular building blocks that eventually turn into soot.

The soot surface grows after nucleation while reaction at the surface occurred. The soot particles began to coagulate after the surface growth. At high temperature the coagulated particles begin to oxidize or losses electron then the coagulated ones breaks into smaller pieces and so on.

STAR-CCM+ uses soot moment and two-equation models to calculate soot formation. The soot moment model has used the method of the moment used to calculate the soot particle size distribution function. For example, the zeroth moment is related to the mean number density and the first moment is to the mean volume fraction of the soot particles. Transport equation has been used to solve these moments [9, 30, 38].

3 Methods

For CFD analysis on the vortex flow solar reactor, the following procedures that are shown in Figure 11 was done in STAR-CCM+ software.

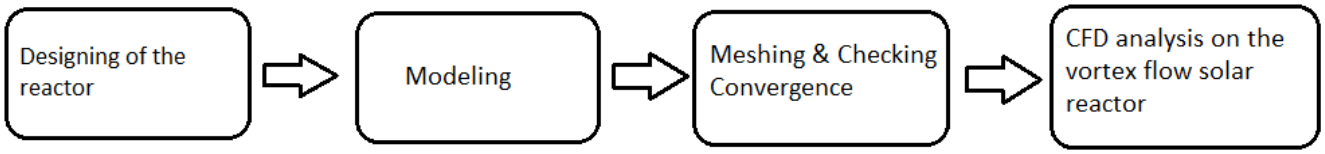

Figure 11: Procedures for CFD-simulation in STAR-CCM+.

3.1 Designing of the reactor

The designing of the vortex flow solar reactor was the first step in STAR-CCM+ for CFD analysis. The reactor was designed like a cylindrical tube, that was placed horizontally. Most of the dimensions of this reactor were taken from Hirsch and Steinfeld's paper and are shown in Figure 12.

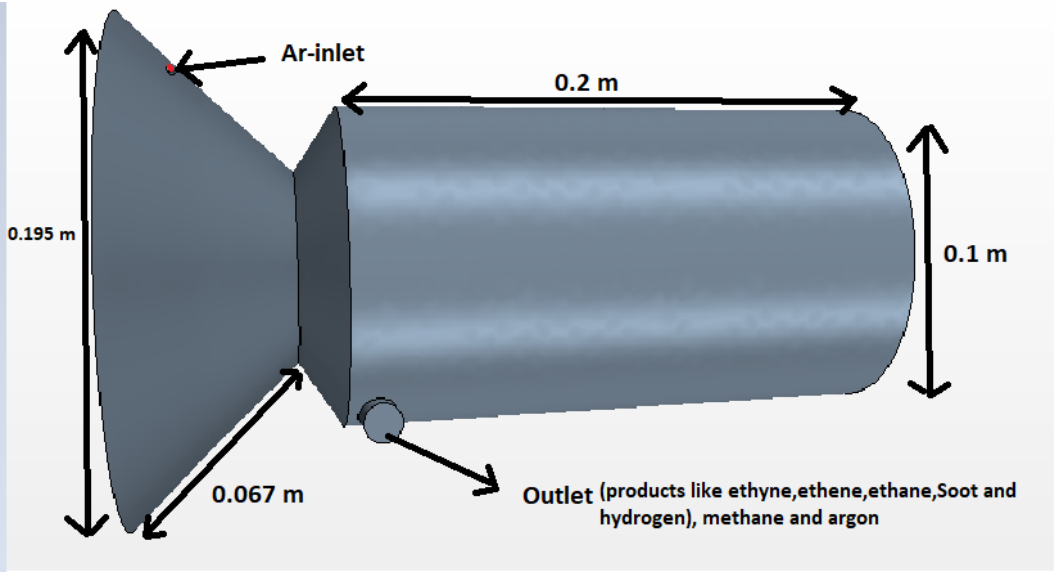

Figure 12: Dimensions of the vortex flow solar reactor.

As shown in Figure 12, Ar was injected at the left-side of the reactor. The diameter of Ar inlet and outlet ports was 0.0016 and 0.010 m, respectively. Methane inlet's port is not shown in Figure 12, because the port was placed in two ways, where it was designed

at the rear and the front of the reactor. This is explained in section (3.1.1) and (3.1.2). Products like C_2H_2, C_2H_4, C_2H_6, H_2, soot with Ar and CH_4-rest, flow out through the outlet port.

3.1.1 Methane inlet at the rear side of the reactor

As shown in Figure 13, methane inlet's port was placed at the rear side of the reactor. The diameter of this port was 0.080 m.

The rear inlet port was designed in two different ways to analyze, which system results in a better performance in a formation of a swirl/vortex flow. These two ways are illustrated in Figure 13, where (a) is a system where the inlet port was placed in a tangential way with a semicircular inlet and (b) is a system where the inlet port was placed normal to the main reactor tube with a full circular inlet. For the case where the inlet port was placed at the rear side, the outlet port was placed at the front side.

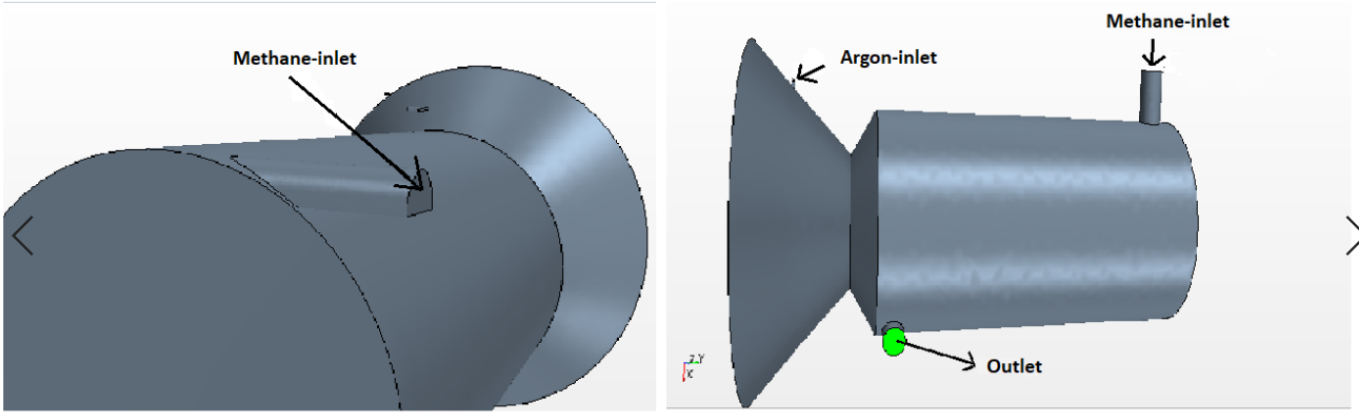

Figure 13: Methane inlet at the rear, where (a) is in the tangential direction and (b) is in the normal direction.

3.1.2 Methane inlet at the front side of the reactor

At another way of configuration, the inlet was placed at the front side of the reactor as illustrated in Figure 14.

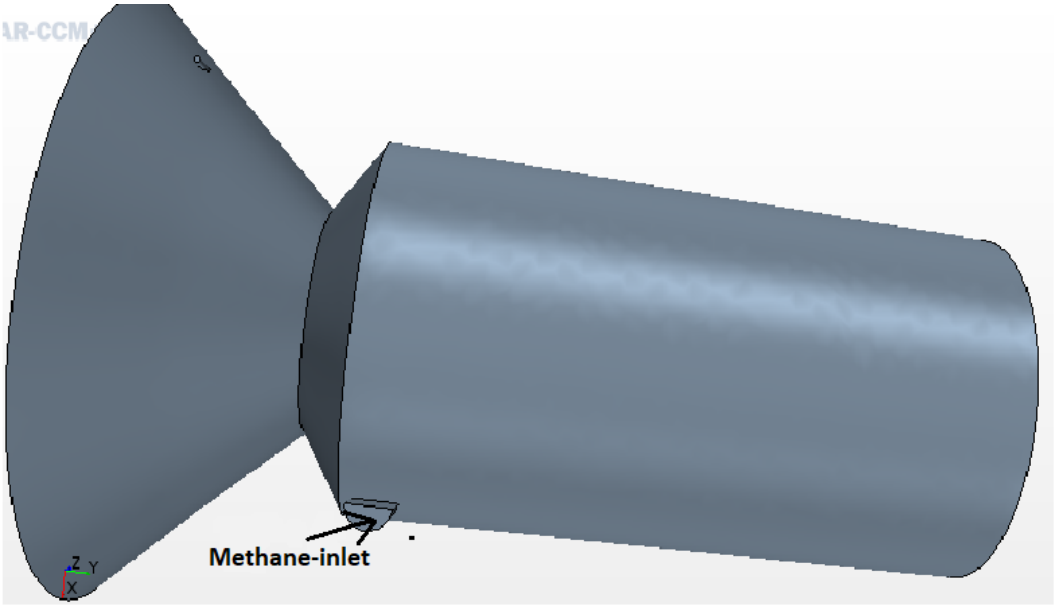

Figure 14: Methane inlet at the front side of the vortex flow solar reactor.

The outlet port was designed at the rear for the case where the inlet port of methane was placed at the front. The outlet and inlet ports was oriented tangentially for this part.

3.1.3 The position of the Ar-inlet port and the inside view of the reactor tube

The inlet port of the Ar-gas is placed at the front but it was positioned in the same configurations as for the methane inlet port as illustrated in Figure 15.

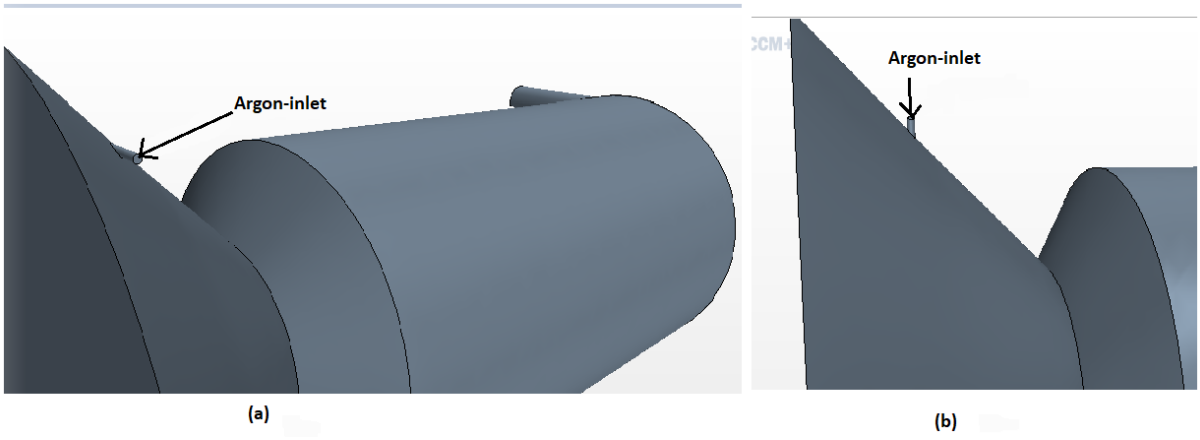

Figure 15: Argon inlet, where (a) is tangential and (b) is vertical inlet ports.

When methane-inlet was placed at the rear and front side of the reactor with tangential position, then the Ar-inlet was placed tangentially. The inside view of the solar reactor that was designed in STAR-CCM+ is shown in Figure 16.

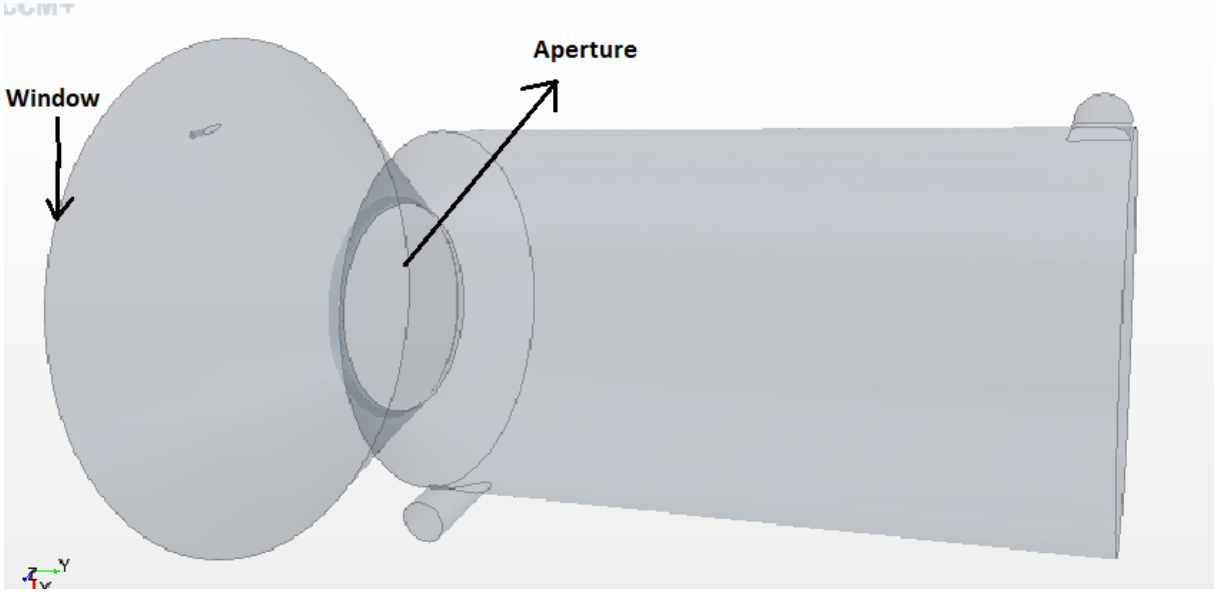

Figure 16: The inside view of the vortex flow solar reactor.

As shown in Figure 16, the aperture was designed with the diameter of 0.06 m. The left-side wall of the reactor is denoted as a "window" in Figure 16. This mimicks the glass window that transmitted the solar irradiation.

3.2 Modeling

The physics models that were chosen in STAR-CCM+ for CFD analysis are turbulent flow in 3D space, ideal gas, reacting, unsteady flow, and soot emissions model.

RANS $k-\epsilon$ model was chosen to simulate the turbulent flow. The reacting species transport model with multi-component gas and a complex chemistry model was selected to deal with reaction transport. The Chemkin files was chosen to model the chemical kinetics in the reaction. The flow was solved by a segregated flow solver. The soot moment model was selected to simulate soot emissions and implicit unsteady was selected to calculate the time marching simulation. A small detail of those selected models was explained in section (2). The time-step for the implicit unsteady was chosen to be 1 ms

because the reaction time was very low.

To model the heat source for the vortex flow solar reactor, the total power that enters to the solar reactor was assumed to be about 5 kW. The heat source was modeled in two methods depending on the condition of concentrated DNI values. The methods are explained in section (3.2.1) and (3.2.2).

3.2.1 Modeling of the volumetric heat source

Norway's DNI-value value was taken as an example to model the heat source in STAR-CCM+ as mentioned in section (1.2). The DNI value in Norway during the summertime can reach up to 200 W/m^2. This DNI needs to be concentrated in the solar concentrator. To estimate, how much of this 200 W/m^2 can be concentrated before it sends to the window of the solar reactor, some values that can help to estimate was taken from Rodat et al. work. The concentrated DNI was estimated as shown in the following.

A typical solar concentrator is able to concentrate irradiation-1000 W/m^2 (1 sun) to 9000 suns. Assuming the DNI-value of Norway (0.2 sun), the same concentrator can yield irradiation up to 1800 suns.

The estimated value of the concentrated DNI was assumed to enter and heat up at the window side of the vortex flow solar reactor, as shown in Figure 17.

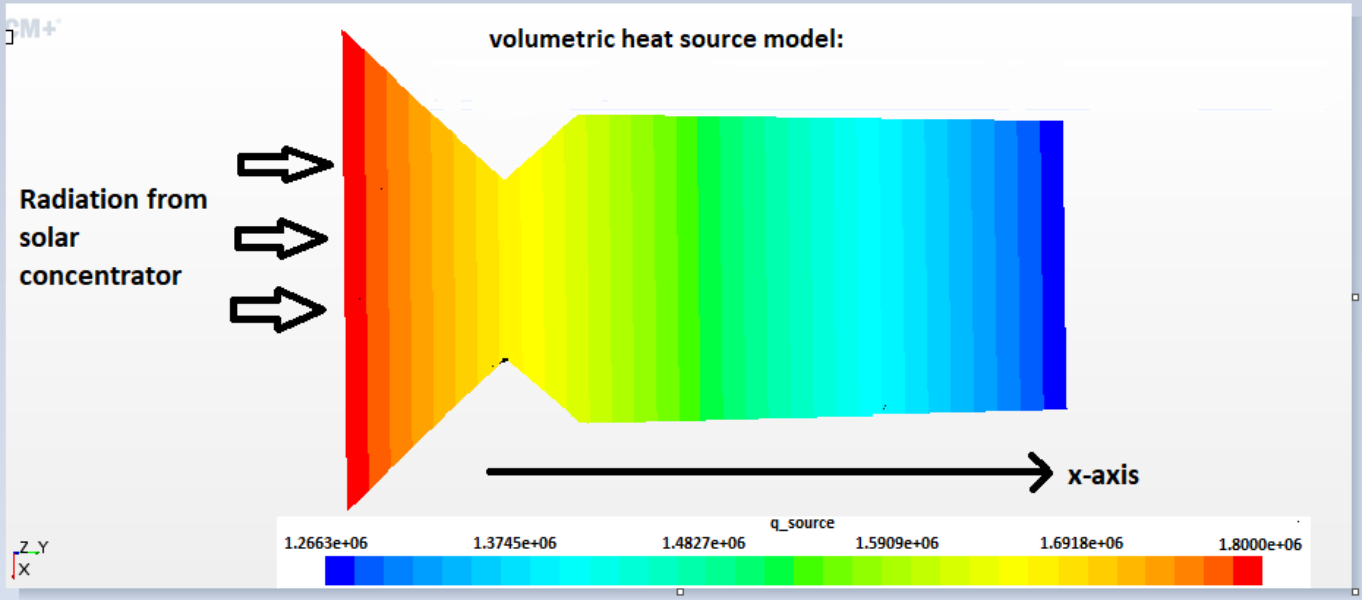

Figure 17: A scene of the volumetric heat source.

To model the heat source as a volumetric, it was taken from the concept of equation (14) or Beer Lambert's law, where the radiation that goes through a transparent medium reduces its intensity with the distance travelled through the medium. With this concept in mind, the mathematical model of the volumetric heat source model that was implemented is expressed as:

$$Q_v = -k \cdot I_0 \cdot e^{-k \cdot x} ,$$

where Q_v (W/m^3) is the volumetric heat source, k (m^{-1}) is the absorption coefficient, I_0 is the DNI (W/m^2), and x is the horizontal length (x-axis) of the reactor as shown in Figure 17.

In this model that is shown in Figure 17, the highest absorption coefficient of methane was chosen to be 1 m^{-1}. This value was taken from Grundy et al.'s paper as mentioned in section (2.8). The highest value of the absorption coefficient was taken to decrease the simulation run time by increasing the temperature rate. For the CFD analysis, the simulation was chosen to stop when the reactor temperature reaches up to 2500 K. The more heat was added to the reactor, the faster it reached 2500 K, therefore the highest absorption coefficient was chosen to assume that all the concentrated solar irradiation equal to 1800 suns got absorbed by methane gas.

The value of $18 \cdot 10^5$ in the model represented the estimated value of concentrated DNI (1800 suns) and multiplied by the absorption coefficient to get volumetric heat (W/m^3). This estimated value of the concentrated DNI (1800 suns) was assumed to travel through the area of aperture with the diameter of 0.06 m. From this, the power that enters to the reactor was 5 kW, after it was calculated by multiplying the cross-section area of the aperture with the concentrated DNI value.

3.2.2 Modeling of heat by a combination of volumetric and electric heat source

The second method of modeling heat source for CFD analysis was to add heat source over some area of the wall of the reactor when it was low DNI. A typical DNI value in Norway is around 100 W/m^2 in the wintertime. The concentrated DNI value for this was 900 suns. This gave a power of about 2.5 kW to enter the aperture area and was calculated using the cross-section area of the aperture. To reach 5 kW, an additional 2.5 kW from electricity was added. The heat by conduction was modeled as for electricity.

The 2.5 KW from the volumetric heat source was done the same procedure as shown in Figure 17 but for this case, the concentrated DNI was 900 suns.

To heat some area of the wall by heat conduction, the heat source was modeled as a heat flux that goes to the wall. The area of the wall that is going to be heated was chosen to be about 0.07 m^2. To estimate, how much heat flux was needed, 2500 W was divided by the area (0.07 m^2). From this, the calculated value of heat flux was 36 suns. This was modeled and illustrated in Figure 18.

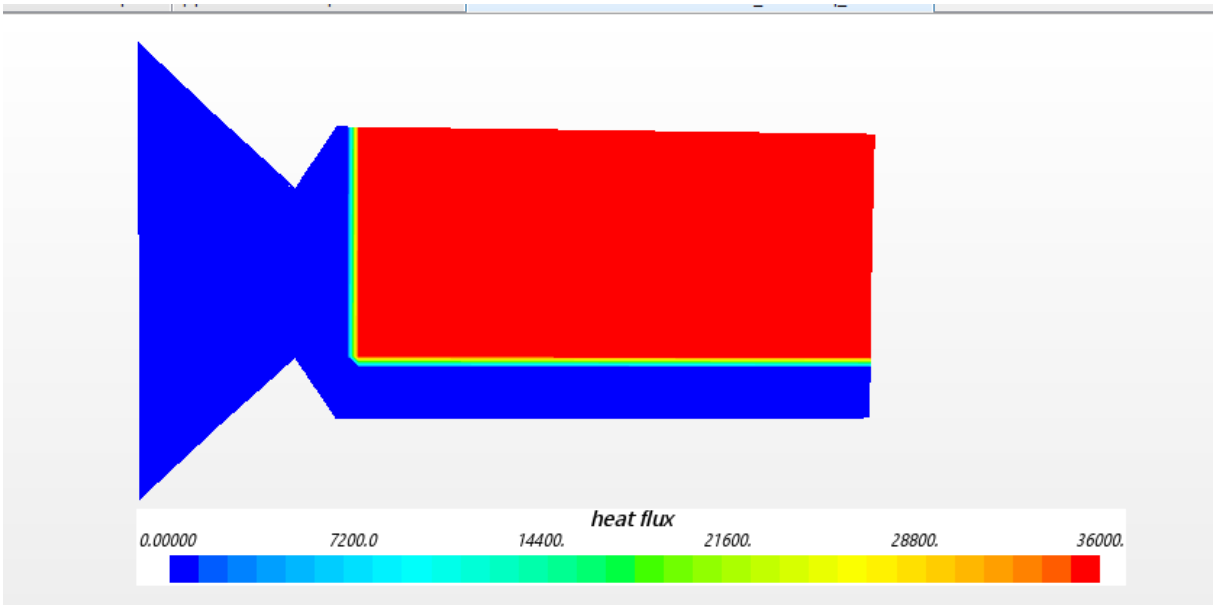

Figure 18: A scene of heat flux to the wall.

As illustrated in Figure 18, the red color represents the region of the wall that was heated. This was an illustration of that some areas that was assumed to heat up by another heat source other than radiation.

3.3 Meshing and checking convergence

To discretize the geometry of the vortex flow solar reactor, a meshing model was generated as described in section (2.3). For these three different types of meshing were tested: polyhedral, tetrahedral, and hexahedral. The polyhedral mesh was the best way to discretize than tetrahedral and hexahedral meshes for this geometry. The reason was that hexa and tetrahedral meshing had some difficulties in the curved area of this geometry. The polyhedral meshed geometry is illustrated in Figure 19.

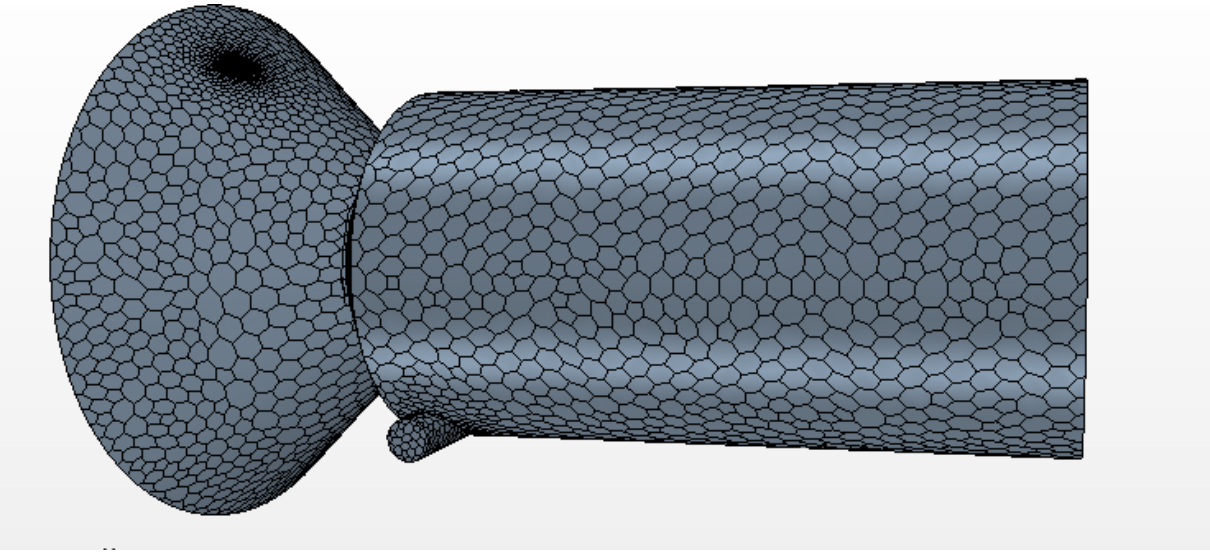

Figure 19: Polyhedral mesh.

3.3.1 Investigation of the mesh size dependency

Three different sizes of polyhedral mesh are simulated and investigated, and these sizes were classified as large, medium, and small. The base size and number of cells to those classified is shown in Table 1. The quality of the thee mesh sizes was checked by comparing their cell quality and skewness angle. The results of these are shown in Table 1.

Table 1: The result of checking mesh quality, base size, and number of cells.

Mesh size	Cell quality	Skewness angle	Base size	Number of cells
Large	Highest:0.86 Lowest:0.0081	84.3^0	0.007	24660
Medium	Highest:0.88 Lowest:0.014	81^0	0.006	29362
Small	Highest:0.91 Lowest:0.04	79^0	0.005	36731

As shown in table(1), all of the mesh sizes that were chosen had a valid and satisfactory mesh quality for CFD analysis, but the mesh quality improves better when it goes from the large or coarser to small or finer mesh size.

3.3.2 Checking convergence after meshing

As mentioned in section (2.3), finer mesh size has a better accuracy and convergence solution than the coarser mesh size, but it is necessary to use a longer computational time than for the coarser mesh size. Therefore, both convergence and computational time needed to be accounted for to get satisfactory solutions.

Three cases with different mesh sizes were simulated to check the convergence. For this simulation, the turbulent intensity and turbulent viscosity ratio were chosen to be 0.01 and 0.1, respectively as initial conditions. The following values 0.2, 0.01, 0.6, and 0.6 of the relaxation factor were selected for velocity, pressure, segregated energy, and species, respectively. Methane and argon were injected with the mass flow of $1.56 \cdot 10^{-5}$ kg/s and $2.71 \cdot 10^{-4}$ kg/s, respectively. The values were taken from Hirsch and Steinfeld work. The mass fraction as the initial condition for methane and argon was also chosen to be 0.5 each.

The velocity vector field for the small and large mesh size was analyzed and shown in Figure 20. This was 40 minutes after simulation started. The inlet port was at the rear with the tangential inlet of methane.

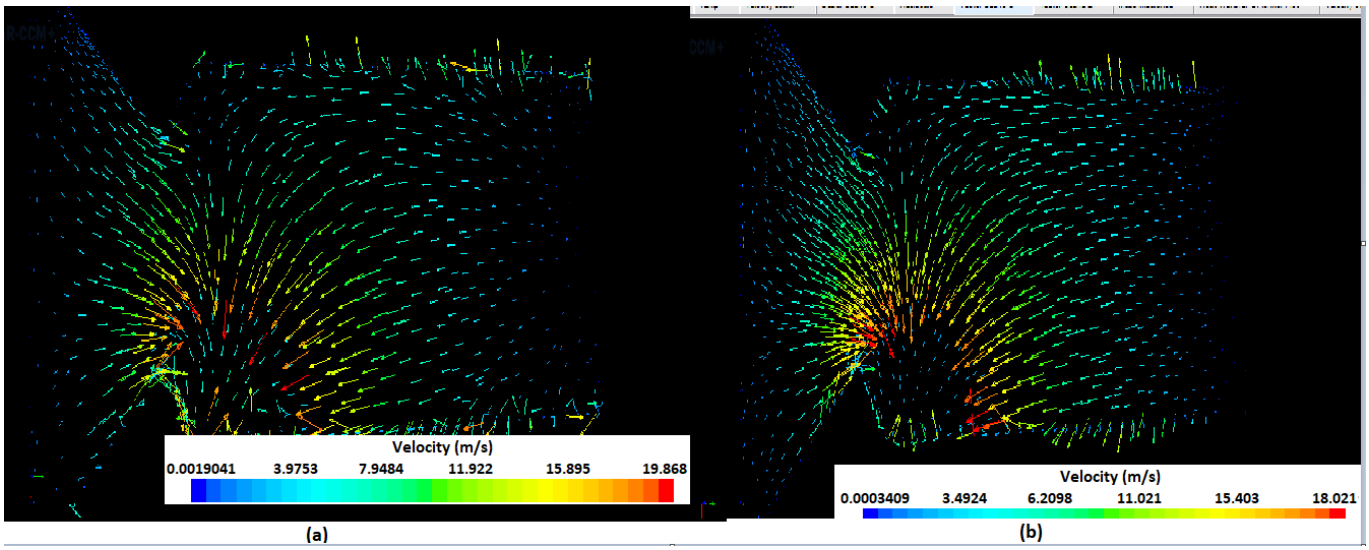

Figure 20: Velocity vector field of methane and argon flow, where (a) is in large or coarser mesh size and (b) is in small or finer mesh size.

As shown in Figure 20, more vector field appeared in the scene with small than the large

mesh size. This means it gave more information of velocity on the area that was going to be analyzed with small than large mesh size, but it took a longer computational time. The temperature of the reactor was also plotted as a function of simulation time for those three mesh sizes as shown in Figure 21. The temperature increased with time in all those three mesh sizes. The temperature rate was higher for the larger than the smaller mesh size. This was because the larger mesh size had a lower number of cells than the smaller mesh size. The equations that represent the physical properties like temperature and velocity were solved in those cells or control volumes, and therefore the small mesh size had a better accuracy than the larger mesh size.

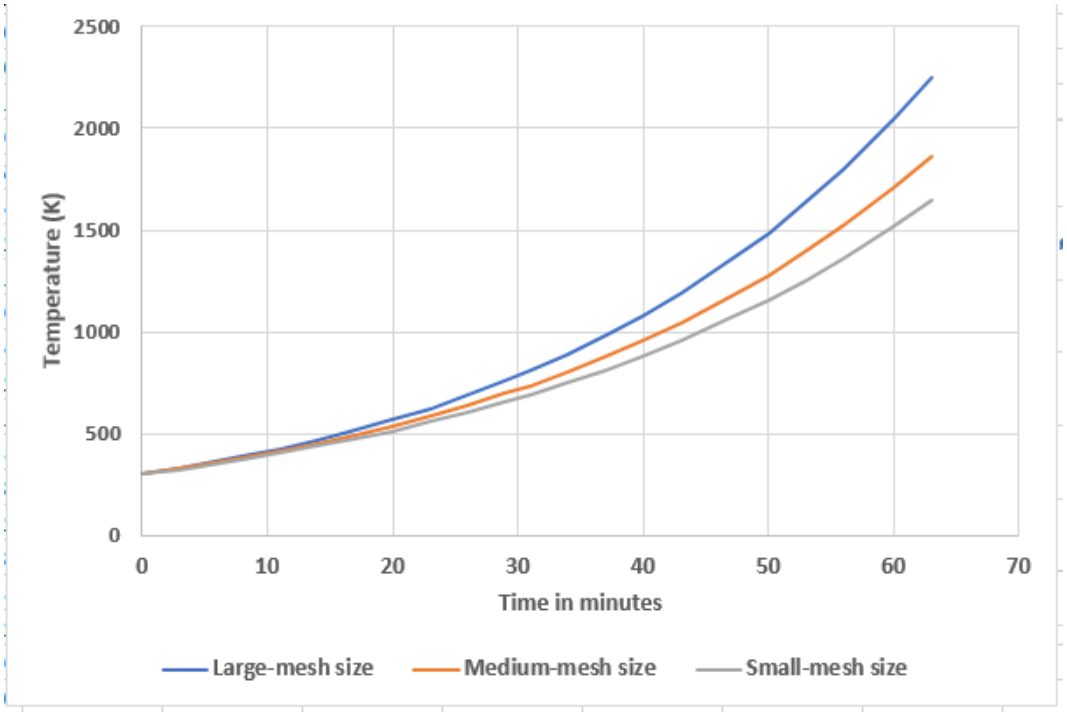

Figure 21: The temperature as a function of time for large, medium and small mesh size.

The solution converged well with the small, medium and large mesh size. To check up the convergence the residuals or errors of the solution, heat, and mass balance were investigated. Figure 22 shows the residuals of all species.

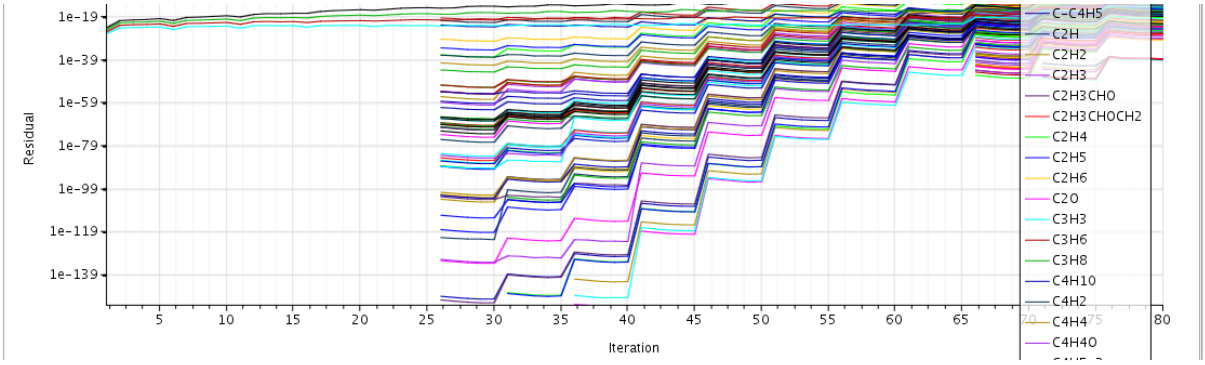

Figure 22: The residuals in every iteration steps for all species in the reaction.

Residuals with less than 1, appear to be an indication of convergence solution, as mentioned in section (2.3).

Heat and mass balance was also observed during simulation run-time. The heat and mass balance for the medium mesh size is illustrated in Figure 23 and Figure 24, respectively.

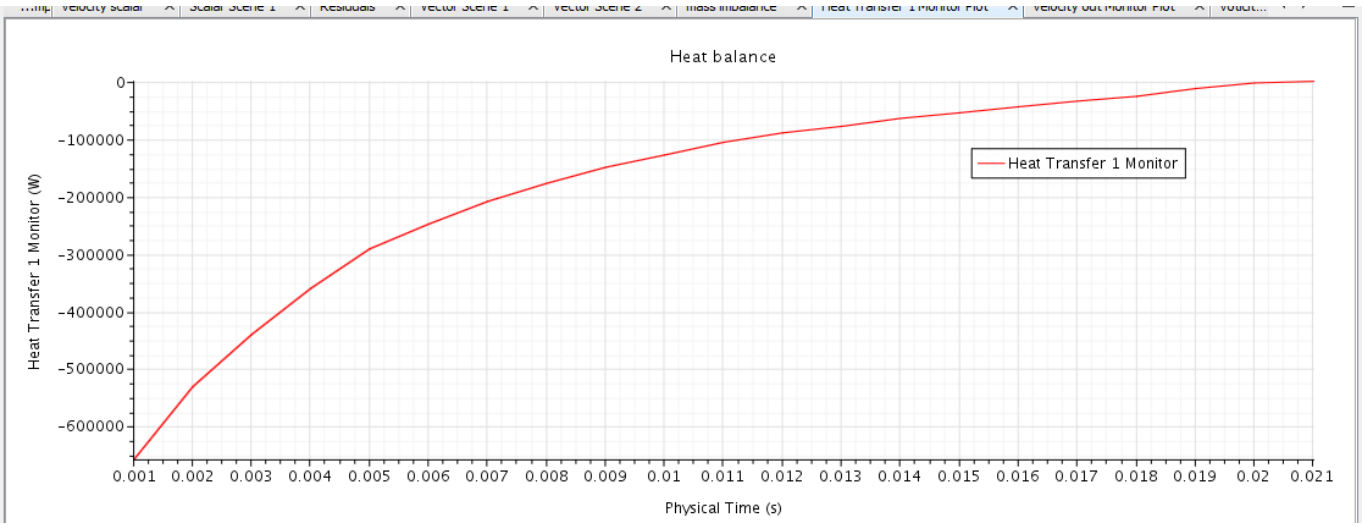

Figure 23: The heat balance.

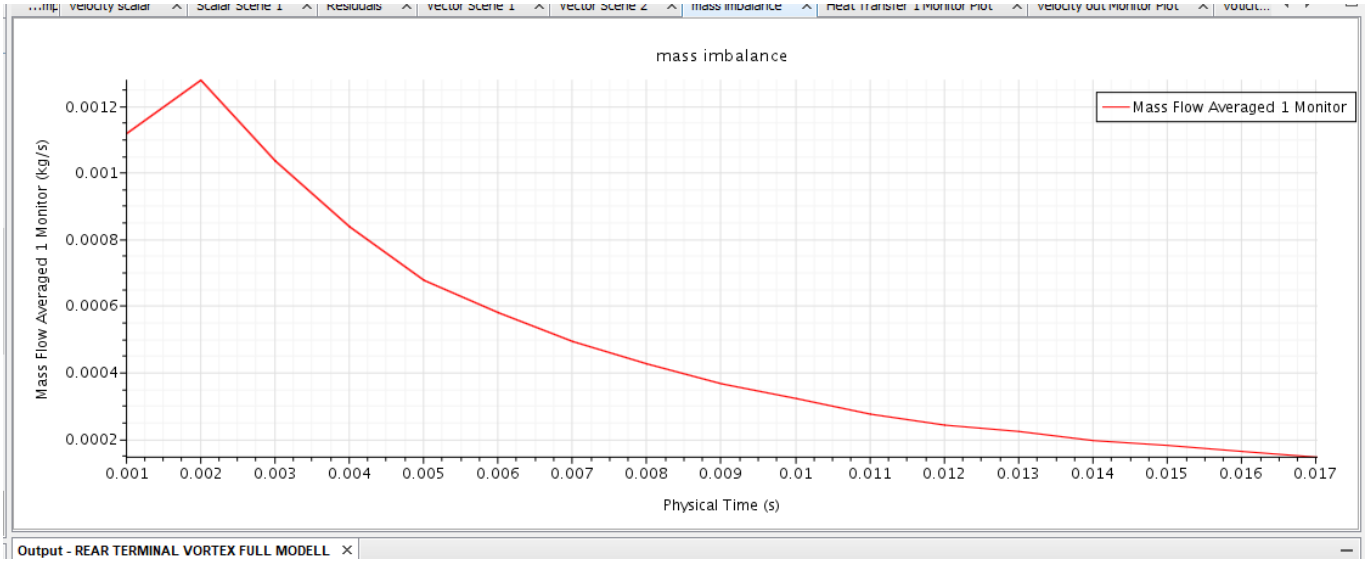

Figure 24: The mass balance.

The heat and mass balance has to be close to 0 if the solution is converging as mentioned in section (2.3). Thus, the result that is shown in Figures 23 and 24 was as expected. The mass, momentum, and energy is conserved, the total mass and energy that enters the reactor has to be equal to the total that comes out, and therefore, the mass and heat balance has to approach 0.

After all the three mesh sizes investigated, the medium mesh size was chosen for CFD analysis because, it gave a reasonable convergence and computational time.

3.4 CFD analysis

After desirable mesh size was chosen, the CFD analysis on the designed geometry of the vortex flow solar reactor was done. Results for CFD analysis were collected by running simulation up to a desirable temperature of the reactor and time. In the CFD analysis, those which was analyzed on this vortex flow reactor are:

- The temperature distribution in the reactor was investigated in the temperature scene.
- The behaviour of the flow for the case where the methane inlet port was placed in the tangential and normal direction was analyzed.

- The outlet temperature for the case where methane inlet was placed at the rear and at the front was compared. The result was also compared with the configuration of 1 and 3 of Hirsch and Steinfeld's research.
- The mass fraction distribution of methane, argon, and hydrogen were investigated. Without argon injection was also investigated.
- Outlet temperature and mass fraction of the products was analyzed with the variation of the absorption coefficient of methane.
- Soot formation was also investigated.
- The temperature distribution, where there was an additional heat source was analyzed.

4 Results and Discussion

The results of the CFD analysis on vortex flow solar reactor are presented and discussed by using some of the concepts that are mentioned in section (2) and compared with some experimental research by others. The results in the following sections was obtained after the simulation run for 80 minutes. The simulation stopped after the highest temperature of the reactor reached 2500 K. The volumetric heat source was also chosen to get the results that are presented in section (4.1) - (4.6). The volumetric and an additional heat source was chosen to achieve the result shown in section (4.7).

4.1 Temperature distribution of the vortex solar reactor

The present section shows the temperature distribution in the cross-section of the reactor. The tangential inlet of methane at the rear side of the reactor was chosen. Argon was also injected tangentially for this part of analysis.

The temperature distribution ranges at the start of the simulation time were as shown in Figure 25, where Fig. 25 a depict the temperature range of 302 - 336 K and Fig. 25 b show 304 - 350 K. The temperature ranges was obtained 4 and 6 minutes, respectively after the simulation started.

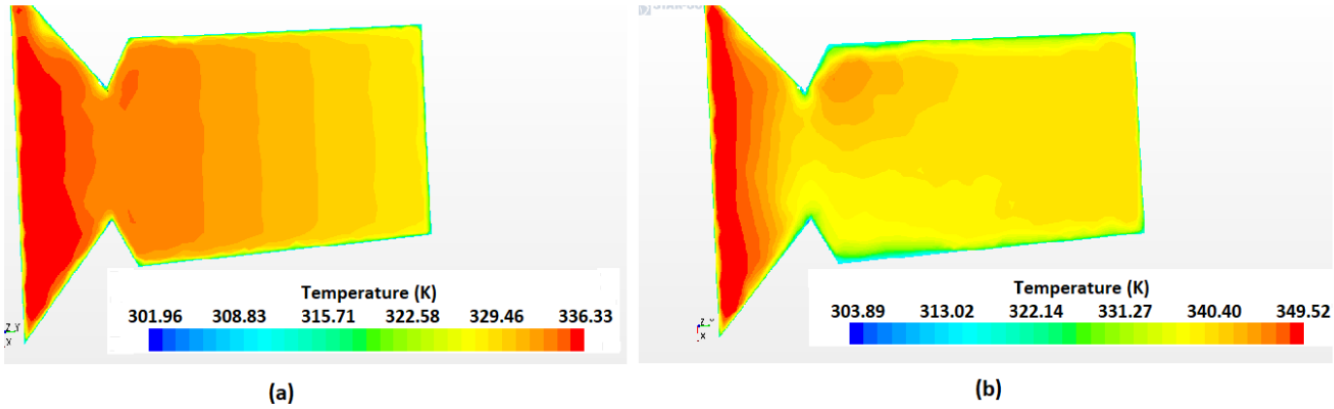

Figure 25: Temperature distribution for two ranges: (a) 302 - 336 K (after 4 min), and (b) 304 - 350 K (after 6 min).

As shown in Figure 25, the temperature over the whole reactor domain increased with

time. From the snapshot presented in Figure 25 a, it was obtained that the temperature decreased from the left-side to the right-side of the reactor. This was because the heat flux that goes through the window, reduced the intensity with the distance traveled through the medium. This agrees with the concept of Beer Lambert's law.

Figure 26 show the temperature ranges, where (a), (b), (d) and (e) was detected after 32, 42, 55, and 77 minutes, respectively.

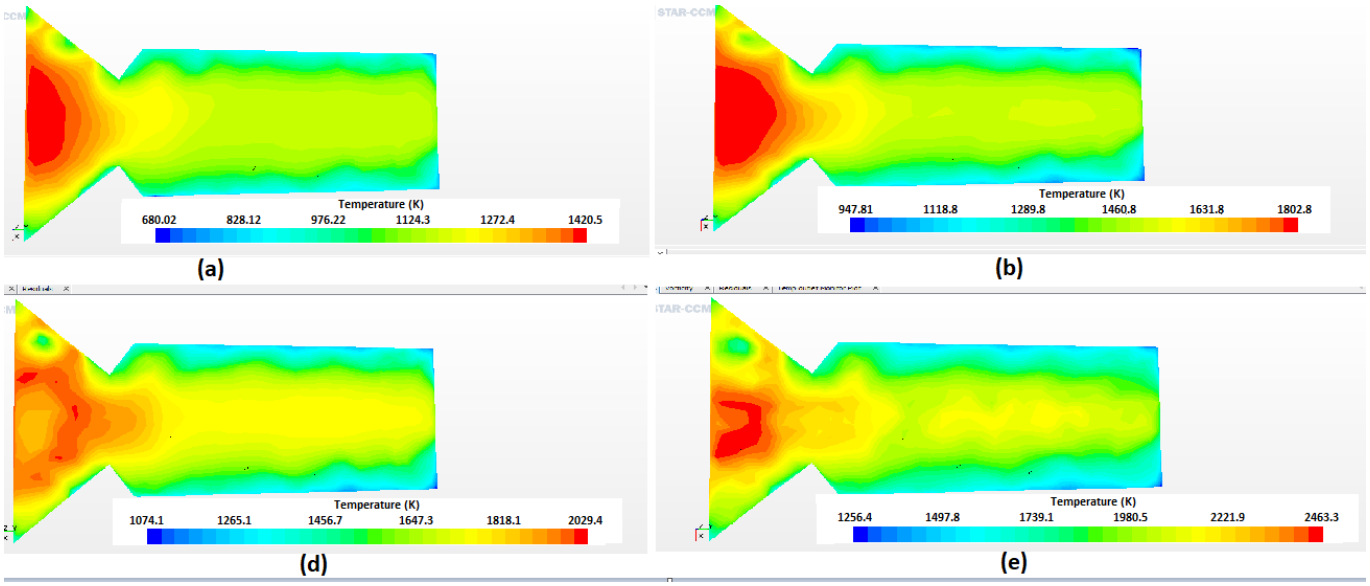

Figure 26: Temperature distribution ranges, where (a), (b), (d), and (e) show in the range of 680 - 1420 K (after 32 min), 948 - 1803 K (after 42 min), 1074 - 2029 K (after 55 min) and 1256 - 2464 K (77 min), respectively.

The temperature range above 1074 K was distributed in a more complex way, where high temperature was detected only at the middle of the left side. One of the reasons was that heat transfer due to convection, diffusion, and others was taken into account, where colder gases diffuse into the reactor.

The temperature distribution snapshots shown in Figures 25 and 26 agreed with the experimental investigations by Rodat et al., Abanades & Flamant, and Hirsch & Steinfeld, where the temperature of the reactor increased with time. This also agreed with the CFD analysis by Ozalp et al., where the temperature of the vortex flow solar reactor increased with time over the entire reactor. The highest temperature was detected, where the heat

flux entered in the Ozalp et al.'s analysis, and this was also agreed with the result shown in Figures 25 and 26.

4.2 The effect of the inlet position on the flow

The behavior of the flow, when methane was injected at the rear in the tangential and normal direction was analyzed, as illustrated in Figure 13. Argon was also injected tangentially for the case where methane inlet port was oriented tangential.

The behavior of the flow, for the case where methane and argon were injected in the normal direction is shown in Figure 27. The flow is presented as a streamlines. This was obtained 60 minutes after starting the simulation when the velocity of the flow reached 20-30 m/s.

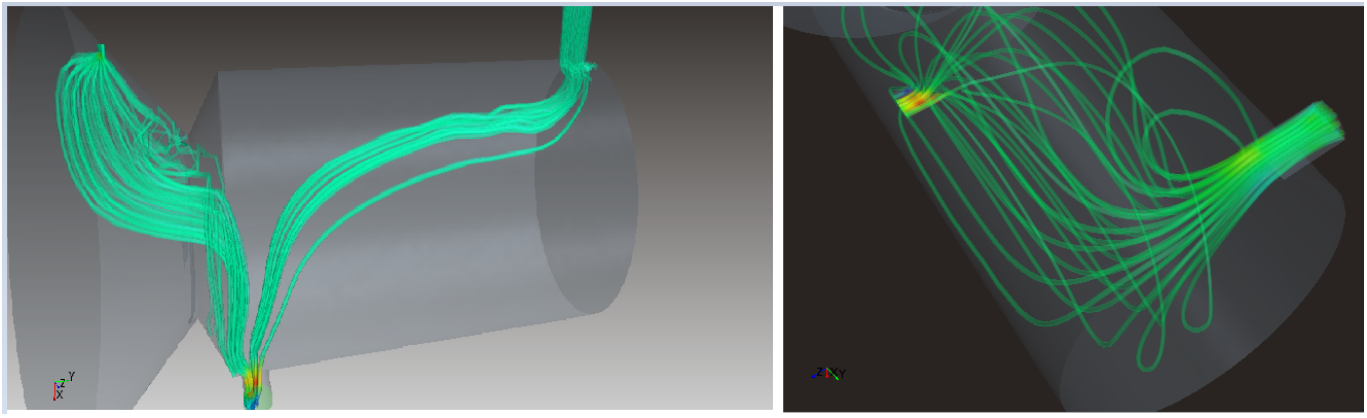

Figure 27: The flow streamlines for the case where argon and methane injected in the normal direction.

As shown in Figure 27, the flow had a small swirl or vortex. The behaviour of the flow for methane and argon tangential inlet method was also presented as a streamline scene, and is shown in Figure 28. This was also occurred 60 minutes after the simulation started when the velocity of the flow reached 20-30 m/s.

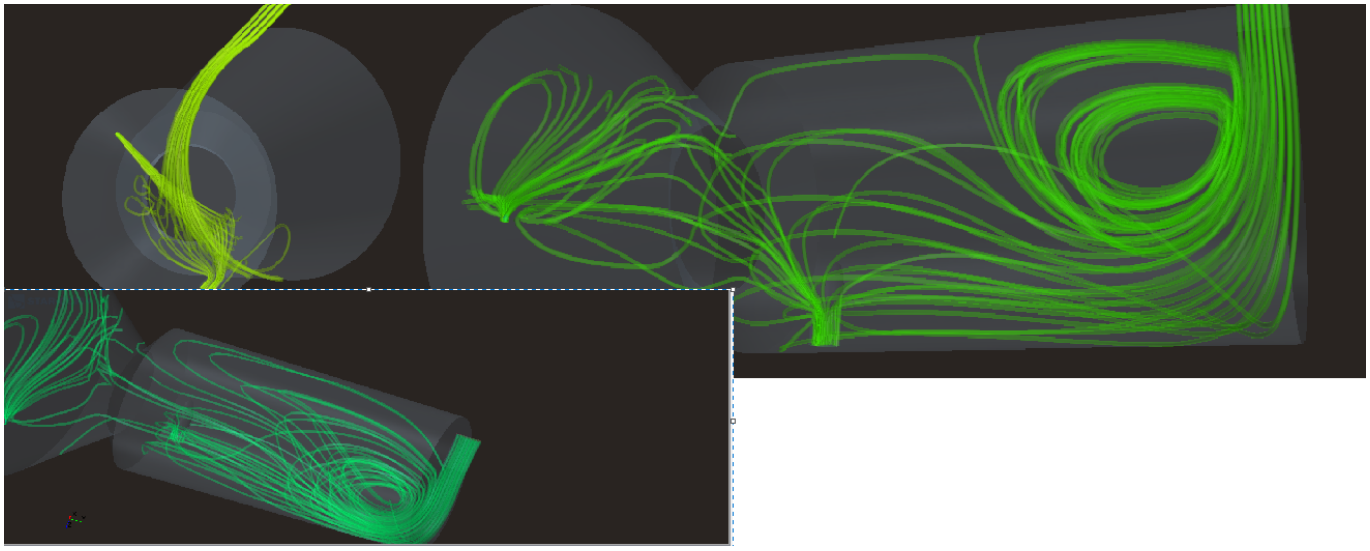

Figure 28: The streamlines of the flow, where argon and methane were injected tangentially.

The behavior of the flow for tangential and normal direction inlet shown in Figures 27 and 28 was compared. The flow swirled more with the tangential inlet than normal direction inlet. This result agreed with the experimental researches and early CFD analysis of Hirsch and Steinfeld, where the inlet injection was tangential to create a swirly flow towards the outlet.

The turbulent dissipation rate and turbulent kinetic energy for tangential and normal direction inlet was also detected during the simulation period. The result of the dissipation and kinetic turbulent energy was plotted against the simulation run-time, as shown in Figure 29. In the figure, (a) is turbulent dissipation rate and (b) is turbulent kinetic energy.

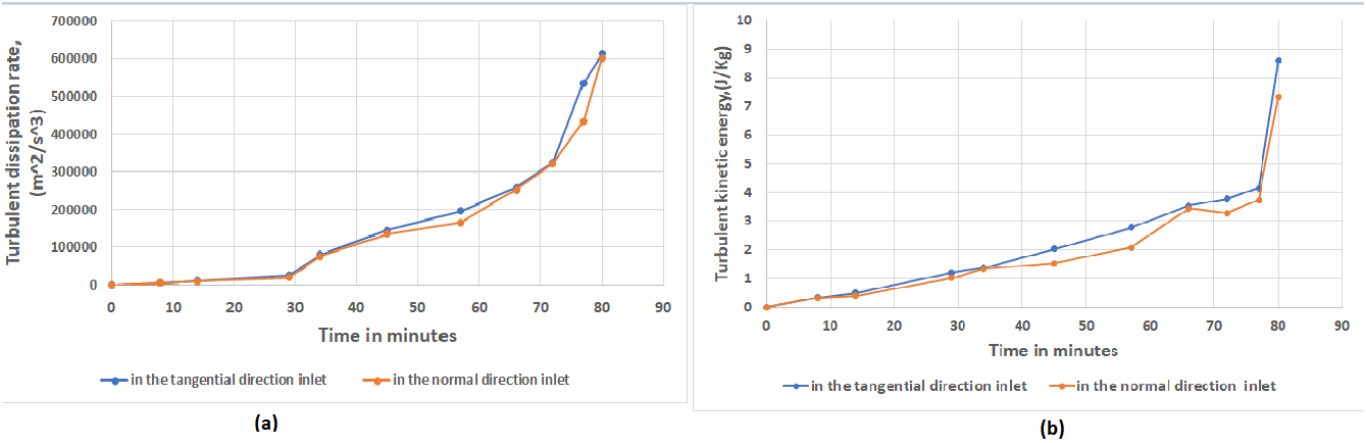

Figure 29: The result of the dissipation and kinetic turbulent energy, where (a) is turbulent dissipation rate (m^2/s^3) and (b) is turbulent kinetic energy (J/Kg).

As shown in Figure 29, both dissipation rate and kinetic energy increased with time. This was due to the increasing of velocity and turbulence in the reactor. The turbulent dissipation rate and kinetic energy for tangential inlet had a higher slope than normal direction inlet. The reason for this was, the flow with swirl/vortex behavior produces more larger eddies than flow without swirl/vortex behavior. These larger eddies have larger kinetic energy and transfer their kinetic energy to the smaller eddies. The smaller eddies dissipate by transferring their kinetic energy to heat energy by viscous forces. Therefore, the dissipation rate and kinetic energy for the tangential inlet method was higher than for the normal direction inlet method. This result also agreed with the CFD analysis of Hirsch and Steinfeld's work by Ozalp et al., where the convective heat transfer was higher for the swirly flow than without. This result also agreed with the concept of the turbulent flow as mentioned in section (2.4).

4.3 The outlet temperature of the rear and front methane inlet methods

The outlet temperature was detected for the case where methane injected at the rear and at the front side of the reactor. Argon was injected tangentially. This part of the research was also compared with the configurations 1 and 3 of Hirsch and Steinfeld's experimental investigation.

The front and rear methane inlet method is illustrated in Figure 13 and 14. The result of the outlet temperature was plotted against the simulation run-time, as shown in Figure 30 after the simulation run for 80 minutes.

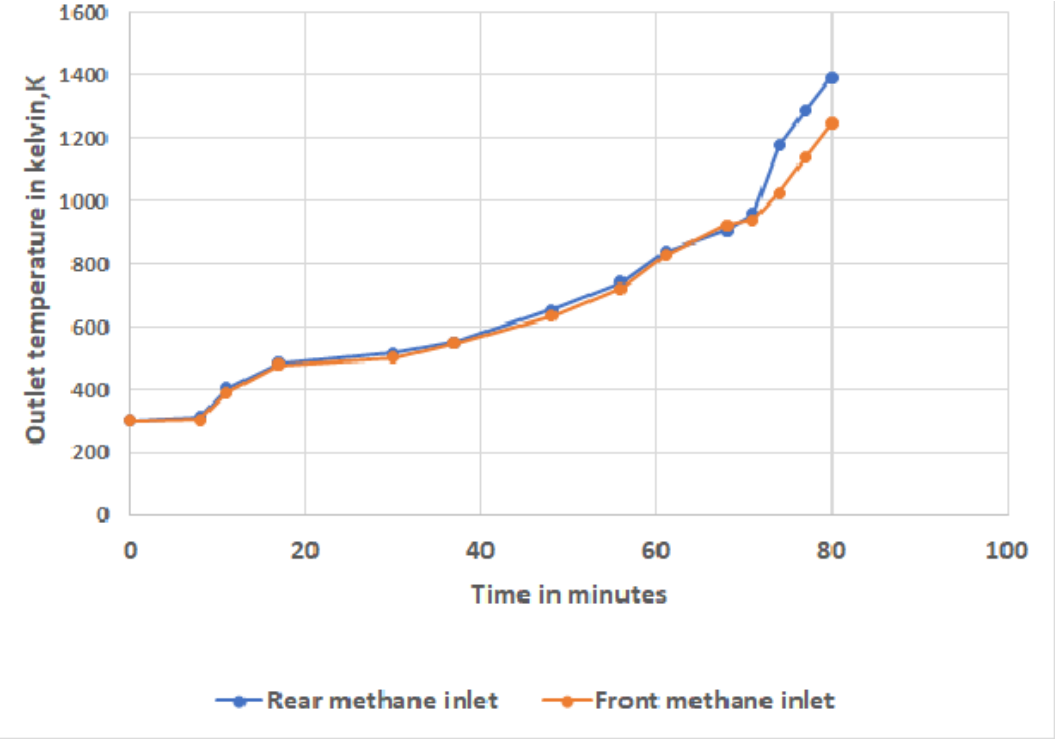

Figure 30: Graph of outlet temperature for rear and front methane inlet methods.

As shown in Figure 30, the outlet temperatures for both front and rear methane inlet methods increased with time. This was one of the indications for the heat flux from solar irradiation distributed over the reactor as expected. This also agreed with Hirsch and Steinfeld's experimental. The outlet temperature for the case where methane inlet placed at the rear was higher than at the front inlet method, and this was also agreed with the Hirsch and Steinfeld's work. The outlet port was closer to the window of the reactor for the inlet at the rear than the front inlet method. Therefore, the outlet temperature was higher for the case where the outlet port was at the front of the reactor.

4.4 The analysis of mass fraction of methane, argon, and hydrogen

The mass fraction distributions of methane, argon, and hydrogen were also investigated and this section show the obtained results.

The purpose of this part of the research was to see if the reaction happened in the region that was far away from the window of the reactor. The tangential methane inlet method at the rear side of the reactor was chosen. The distribution of argon and methane mass fraction as shown in Figure 31 was obtained after 12 minutes.

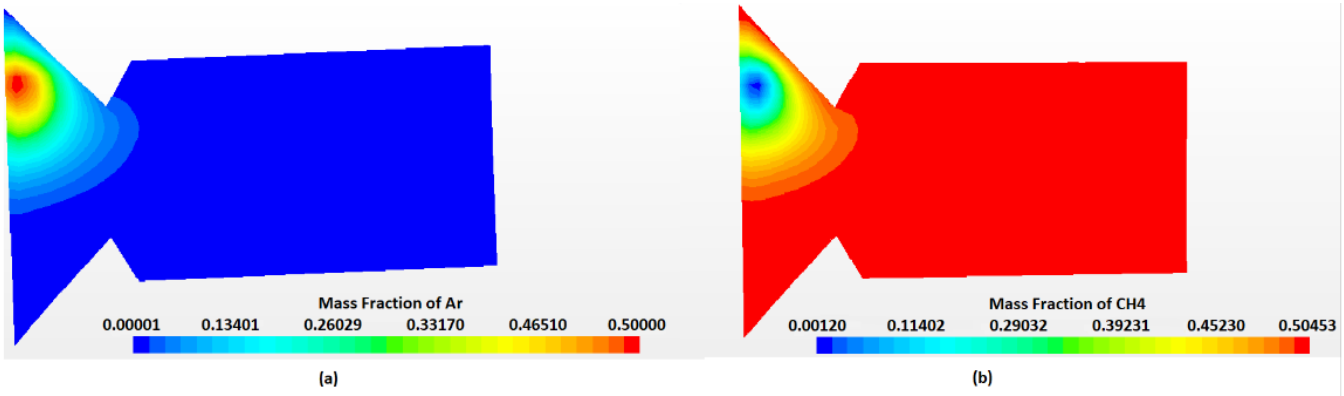

Figure 31: Mass fraction distribution of argon and methane, where (a) and (b) show the snapshots of argon and methane mass fraction, respectively.

The distribution of argon and methane mass fraction are also shown 45 minutes after the simulation started, see Fig. 32. In the figure, (a) and (b) depict the mass fraction of argon and methane, respectively.

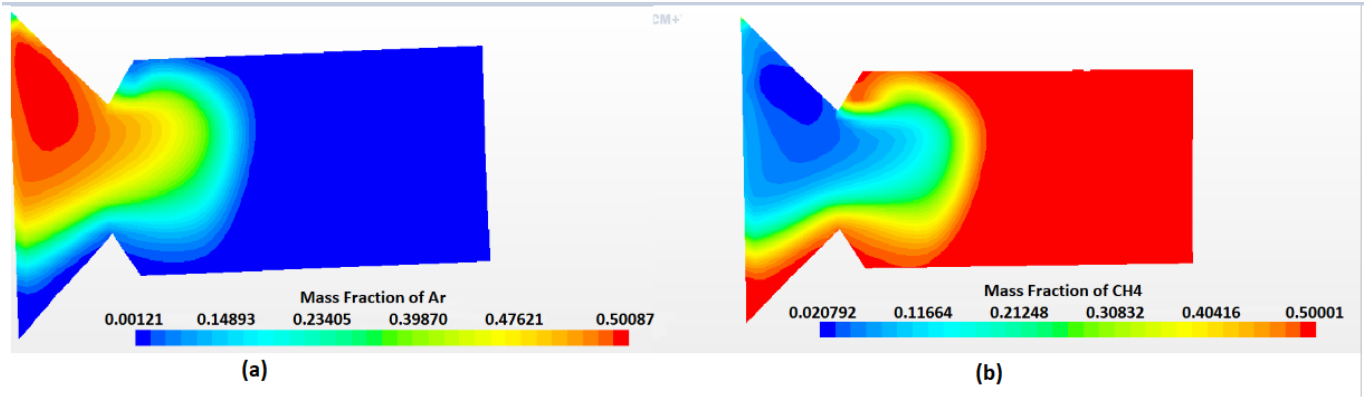

Figure 32: Mass fraction distribution of argon and methane, where (a) and (b) show argon and methane mass fraction, respectively.

Hydrogen which is a final product and methane mass fraction distribution as illustrated in Figure 33 was obtained after 55 min. Fig. 33 a and Fig. 33 b represents methane and hydrogen hydrogen mass fraction.

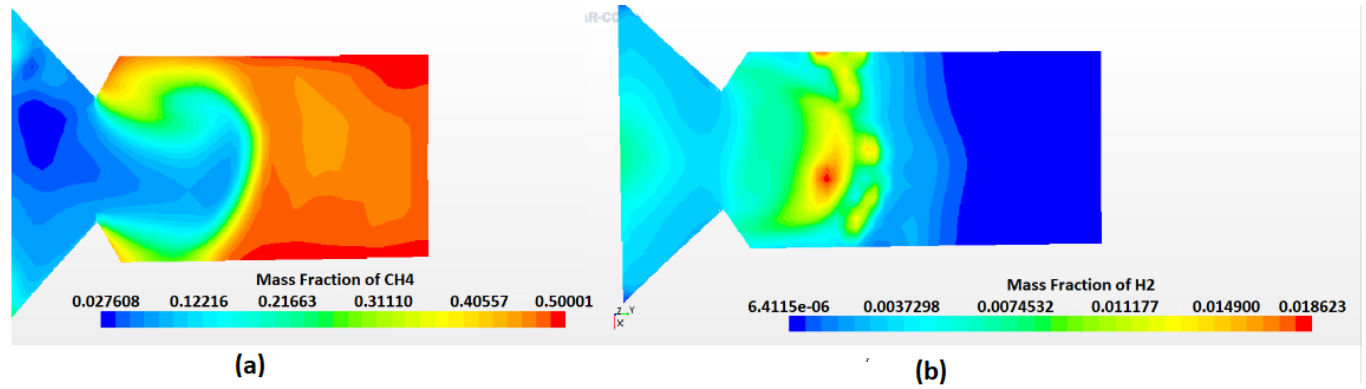

Figure 33: Mass fraction of methane and hydrogen, where (a), and (b) represents methane and hydrogen mass fraction, respectively.

The mass fraction distribution of hydrogen and soot mass density without argon injection were also obtained after 30 min, see Fig. 34. The temperature distribution, and the soot mass density (kg/m^3) were also presented in the figure. Fig. 34 b depict the mass fraction of methane at the start of the simulation time.

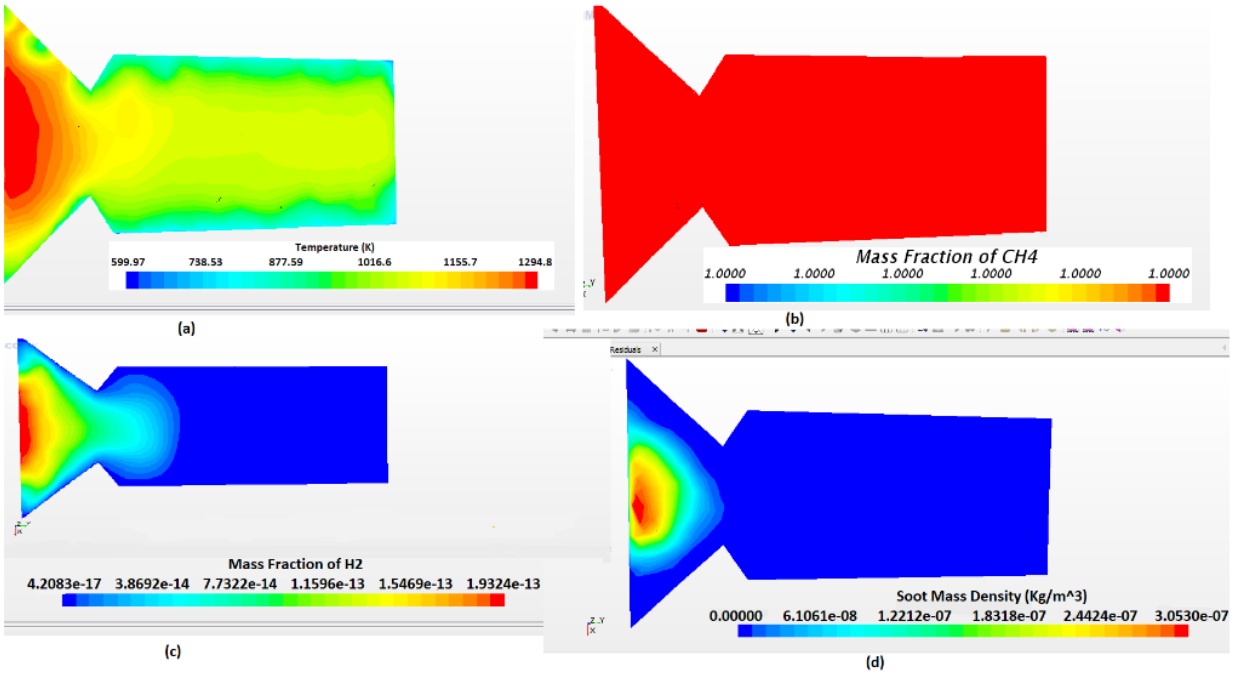

Figure 34: Mass fraction distribution without argon, where (a), (b), (c), and (d) show the temperature of the reactor in the range of 600 - 1300 K, methane mass fraction, hydrogen mass fraction and the soot mass density (kg/m^3), respectively.

As shown in Figures 31 and 32, the mass fraction of argon covered the area near the window. This indicated that methane gas flow was pushed far away from the window by the argon. Argon is an inert or carrier gas, that is used for transport of other gasses and particles. This agreed with Hirsch & Steinfeld's, Abanades & Flamant, and Rodat et al. experimental investigation. It was also agreed with the CFD analysis by Ozalp et al., where it was observed that argon mass fraction was dominant near the window of the reactor. As shown in Figure 33, most of the methane reaction occurred at the middle of the reactor. Therefore, most of the hydrogen seen at the middle, where the temperature was higher as expected. Hydrogen was began to occur 55 minutes after the simulation started and when the reactor temperature was above 1300 K, see Fig. 26 and Fig. 33 b. This result was agreed with the experimental and CFD analysis by Hirsch & Steinfeld, Abanades & Flamant, Rodat et al., and Ozalp et al. Without argon injection, as shown in Figure 34, methane reaction occurred near the window, where the temperature was higher.

4.5 The absorption coefficient of methane

The absorption coefficient of methane was varied to investigate the outlet temperature and mass fraction of the products that is H_2, C_2H_2, C_2H_4, C_2H_6, and soot. The values of the absorption coefficient of methane was chosen on the basis of Grundy et al.'s analysis. In their investigation, the absorption coefficient of methane in the infrared region was detected in the range of 0.01 to 100 cm^{-1}, see Fig. 9. In this research, the absorption coefficient was chosen to be varied inside these ranges as shown in Fig. 9, that is, between 0.17 to 0.97 m^{-1}. A tangential methane inlet method at the rear was chosen. Argon was also injected tangentially.

To analyze the outlet temperature and the products with the variation of methane absorption coefficient, the estimated concentrated DNI (W/m^2) was multiplied by absorption coefficient (k) to model as a volumetric heat (W/m^3) as expressed in equation (15). As mentioned in section (3), the estimated intensity was 1800 kW/m^2.
The outlet temperature with the variation of the absorption coefficient was found, after running the simulation to 2500 K reactor temperature. The simulation time was 80 minutes, and the obtained result is illustrated in Figure 35.

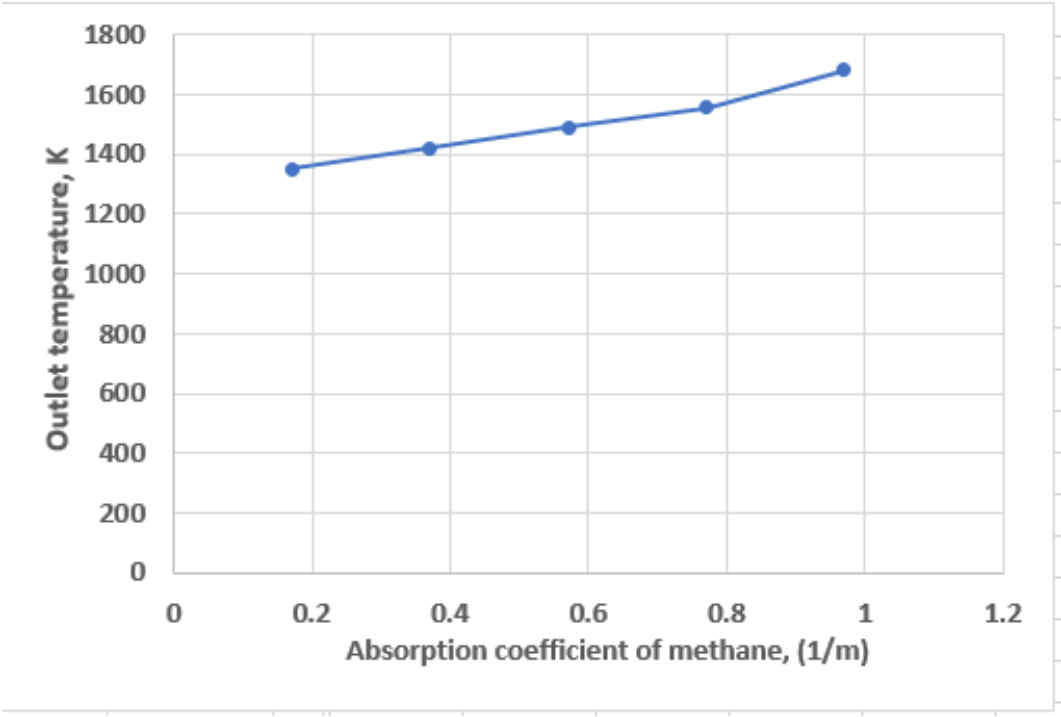

Figure 35: The outlet temperature with the variation of methane absorption coefficient.

Mass fraction of reaction products against the absorption coefficient are shown in Figure 36. In the figure, (a) shows the mass fraction of C_2H_2, C_2H_4 and C_2H_6, and (b) shows the mass fraction of H_2, C_2H_2 and soot number density against methane absorption coefficient. This was also detected 80 minutes after the simulation started.

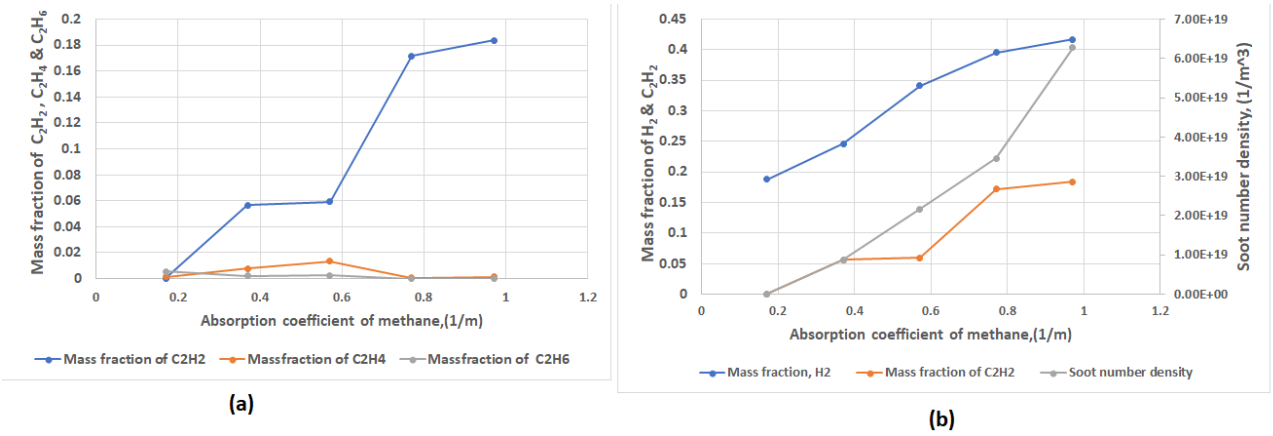

Figure 36: Mass fraction of the gas products and soot number density, where (a) show the mass fraction of C_2H_2, C_2H_4 and C_2H_6, and (b) show the mass fraction of H_2, C_2H_2 and soot number density(m^{-3}) against the methane absorption coefficient(m^{-1}).

According to the results shown in Fig. 35 and Fig. 36, the outlet temperature and mass fraction of the products like H_2, C_2H_2, and soot number density increased with the absorption coefficient. The reason for this was the heat that absorbed by methane gas increased when the absorption coefficient of methane increased. In other words, the absorbed radiation intensity that enters through the window by methane gas increased with the absorption coefficient. This agreed with the concept of Beer-Lambert law, as mentioned in section (2.8). This result also agreed with the experimental research by Hirsch & Steinfeld, Abanades & Flamant, and Rodat et al. and CFD analysis by Ozalp et al. This also agreed with the concept of Arrhenius equation (12) as mentioned in section (2.5.2), where the reaction rate increased with the increasing of temperature.

As shown in Figure 36, C_2H_2, C_2H_4, and C_2H_6 were obtained as products during the simulation run-time. This agreed with the analysis by Hirsch & Steinfeld, Abanades & Flamant, and Rodat et al., where the production of C_2H_2, C_2H_4 and C_2H_6 were observed during the methane cracking process. As shown in Fig. 36 b, hydrogen and soot particles

were mainly seen when the absorption coefficient increased and the outlet temperature was reached in the range of 1300 - 1700 K. This agreed with the analysis of methane pyrolysis by Billaud et al. as mentioned in section (2.7.1), where hydrogen and carbon particles were mainly seen as products above 1400 K. Hydrogen and carbon particles were also seen as a main products in the experimental research by Hirsch & Steinfeld, Abanades & Flamant, and Rodat et al.

4.6 Soot formation

The soot or carbon particles that were occurred as a final product was also investigated. The tangential methane inlet at the rear side of the reactor method was chosen for this part of the analysis. The argon injector was oriented tangentially.

The mass fraction of C_2H_2 and soot mass density (kg/m^3) was analyzed to see if there was a relation between them during the reaction process. The soot and mass fraction of C_2H_2 were investigated 35 minutes after starting the simulation, see Fig. 37. In the figure, (a) and (b) shows the mass fraction of C_2H_2, and mass density of the soot formation (kg/m^3), respectively.

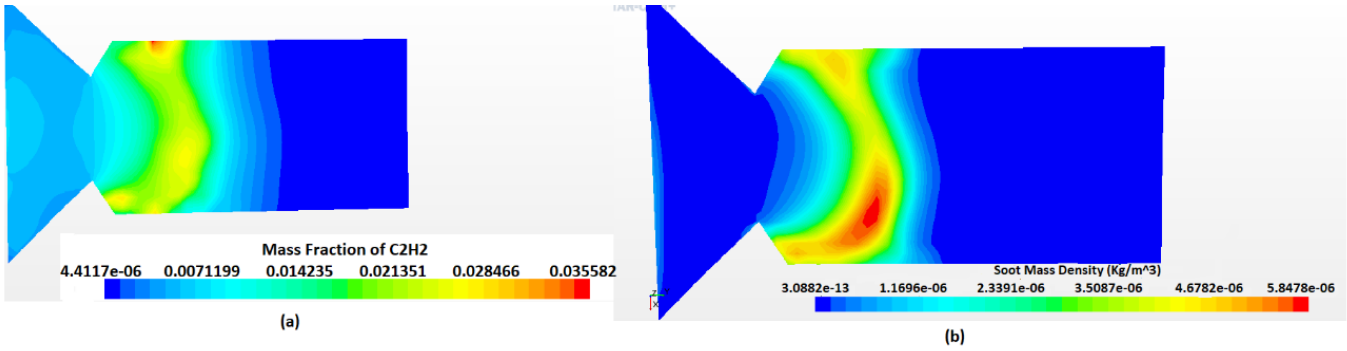

Figure 37: The soot and mass fraction of C_2H_2, where (a) and (b) show the mass fraction of C_2H_2, and mass density of the soot formation (kg/m^3), respectively.

As shown in Figure 37, the mass density of the soot formation was mostly shown in the place where the highest mass fraction of C_2H_2 occurred. This agreed with the concept of soot formation as mentioned in section (2.9), where C_2H_2 is one of the reasons for soot formation. It is also shown in Fig. 36 b, where the production of C_2H_2 increased, the soot

number density also increased. This result also agreed with experimental investigation by Ruiz et al. Due to argon injection near the window, the highest C_2H_2 and soot particles occurred at the middle of the reactor.

The soot diameter was also analyzed. The result is shown in Figure 38, where the diameter (nm) of the soot was plotted as a function simulation run-time (min). This result was obtained after 80 min.

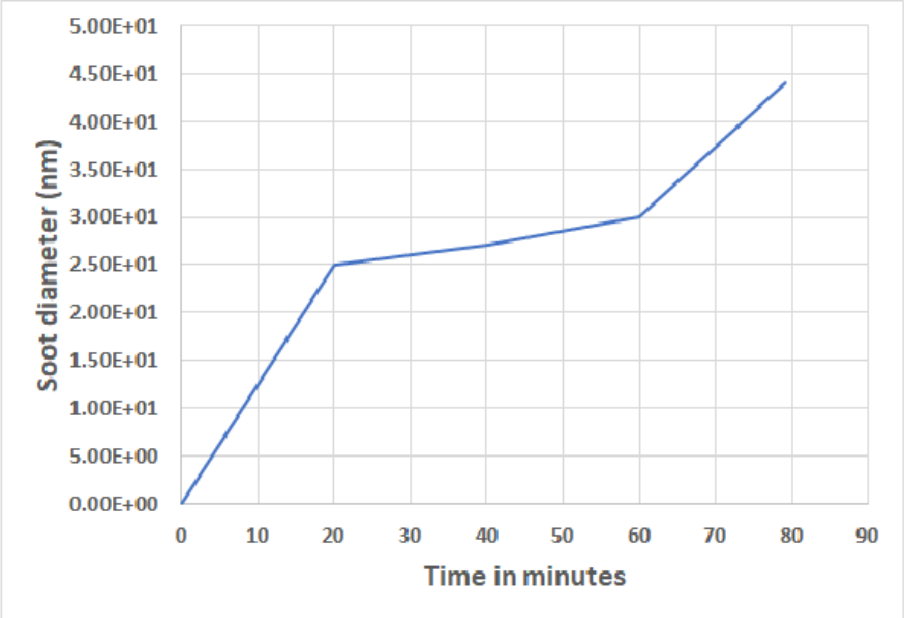

Figure 38: Soot diameter as a funtion of simulation run-time.

As shown in Figure 38, the soot diameter was in the range of 40-10 nm. This was agreed with Hirsch & Steinfeld, Abanades & Flamant, and Rodat et al. experimental research, where the carbon particles diameter was observed in a range of 10-50 nm. The soot diameter was also increased with time as shown in Figure 38. The reason could be as mentioned in section (2.9), where the particle nuclei was produced from PAH before the soot particles formed. This particle nuclei or the initiation steps has a smaller diameter than the soot.

4.7 Temperature distribution, where the heat source was the combination of solar and electricity

The temperature distribution was analyzed, where the heat source was both from solar and an addition heat flux for this part of analysis. The tangential methane at the rear side of the reactor was chosen for this part of the analysis. This part of the research was done without argon also injection. The temperature distribution was investigated by running simulation up to 2000 K for 80 minutes. The result in temperature ranges shown in Figure 39. In the figure, (a), (b), (c), and (d) show in a range of 307- 325.2 K, 352 - 425 K, 613 - 1058 K, and 1165 - 1688 K, respectively. (a), (b), (c) & (d) was detected 10, 22, 34, 65 minutes respectively after starting the simulation.

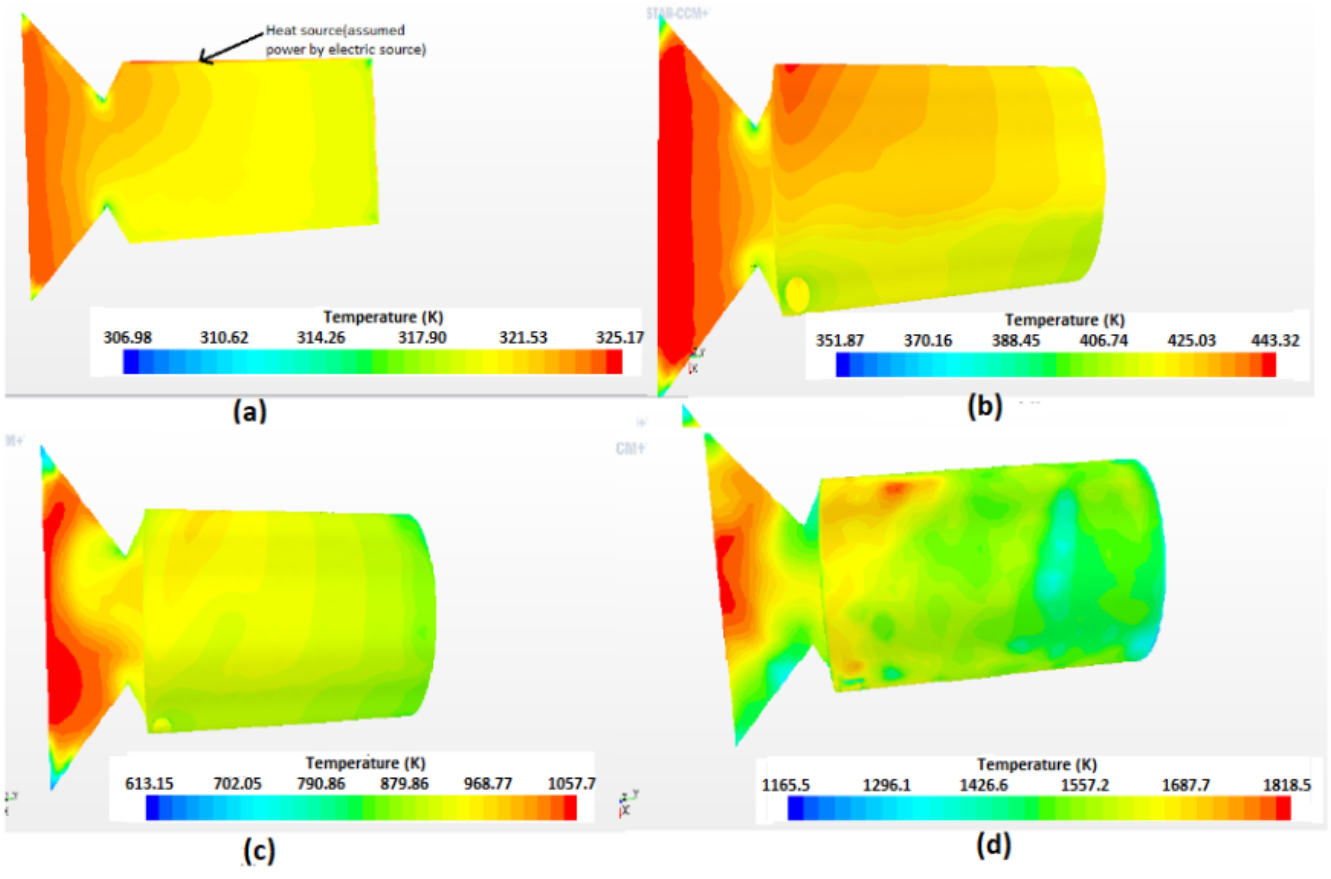

Figure 39: Temperature ranges, where (a), (b), (c), and (d) show temperature ranges of 307- 325.2 K (after 10 min), 352 - 425 K (after 22 min), 613 - 1058 K (after 34 min), and 1165 - 1688 K (after 65 min), respectively.

As shown in Figure 39, the temperature was increased with time as expected. The highest temperature was also detected in the area of the reactor, where the heat sources were placed. As shown in Fig. 39 a, the temperature was higher at the top-middle side of the reactor than the bottom area. This was because of the additional heat flux in that area. This temperature distribution also agreed with the experimental analysis by Rowe et al. The hydrogen mass fraction after 65 min is also depict in Fig. 40.

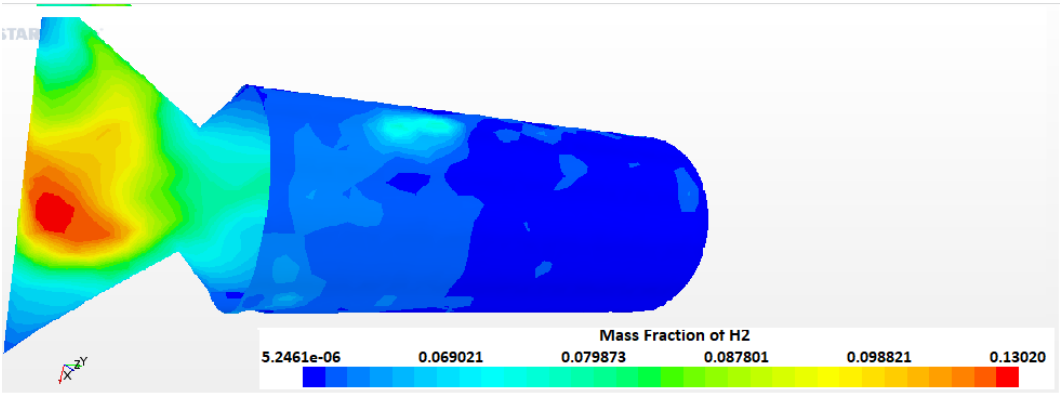

Figure 40: The mass fraction of hydrogen after 65 min.

As illustrated in Fig. 40 and Fig. 39, the hydrogen was occurred in the area, where the temperature was higher. As mentioned in section (4.4), hydrogen produced when the temperature of the reactor reached above 1300 K. This indicated that hydrogen can also be obtained when the temperature reached in the range of 1165 - 1818 K as shown in the figure.

5 Conclusion

In the present analysis, CFD investigation of methane cracking using solar reactor is given. For this CFD research, the Hirsch and Steinfeld's vortex solar reactor was designed. This CFD analysis provides to research the temperature distribution, characteristic of the flow, mass fraction of methane, argon, the products like hydrogen, and soot formation during this methane pyrolysis process. From this analysis, it is understood that hydrogen can be obtained using a vortex solar reactor. The increasing of the reactor temperature above 1300 K permits to intensify hydrogen yield. The tangential inlet port gives a higher vortex flow, and this increases the convective heat transfer of the flow. Argon injection is necessary in the reactor to prevent the window from particle clogging and transport. The products like C_2H_2, C_2H_4, and C_2H_6 can be obtained during the methane cracking process. The outlet temperature can be achieved higher when methane inlet port is placed at the front of the reactor. The amount of the heat absorbed increases with the absorption coefficient. The carbon or soot particles can be also produced as a final products with hydrogen. Based on this CFD analysis the following conclusive remarks can be made: hydrogen can be produced by natural gas pyrolysis using solar energy without carbon dioxide emission. It is also possible to obtain hydrogen, when there is low solar irradiation like Norway by adding heat from electricity in to the reactor.

References

[1] Stephane Abanades and Gilles Flamant. "High-temperature solar chemical reactors for hydrogen production from natural gas cracking". In: *Chemical Engineering Communications* 195.9 (2008), pp. 1159–1175.

[2] Stéphane Abanades and Gilles Flamant. "Experimental study and modeling of a high-temperature solar chemical reactor for hydrogen production from methane cracking". In: *International journal of hydrogen energy* 32.10-11 (2007), pp. 1508–1515.

[3] IPCC Adopted. "Climate Change 2014 Synthesis Report". In: *IPCC: Geneva, Szwitzerland* (2014).

[4] David W. Ball. *Introductory Chemistry*. 2011.

[5] Lenny Bernstein et al. *Climate Change 2007 Synthesis Report*. Intergovernmental Panel on Climate Change, 2008.

[6] Philippe Blanc et al. "Direct normal irradiance related definitions and applications: The circumsolar issue". In: *Solar Energy* 110 (2014), pp. 561–577.

[7] Henning Bockhorn. *Soot formation in combustion: mechanisms and models*. Vol. 59. Springer Science & Business Media, 2013.

[8] Rashmi Chaubey et al. "A review on development of industrial processes and emerging techniques for production of hydrogen from renewable and sustainable sources". In: *Renewable and Sustainable Energy Reviews* 23 (2013), pp. 443–462.

[9] Seung-Hyun Chung. "Computational Modeling of Soot Nucleation." PhD thesis. 2011.

[10] Jim Clark. *Cracking*. (Cited 13-03-2021). Sept. 13, 2020. URL: `https://chem.libretexts.org/@go/page/3877`.

[11] Lars. Davidson. *Fluid Mechanics,Turbulent Flow and Turbulence Modeling*. 2020.

[12] Andrew L Dicks. "Hydrogen generation from natural gas for the fuel cell systems of tomorrow". In: *Journal of power sources* 61.1-2 (1996), pp. 113–124.

[13] S Galvagno et al. "Pyrolysis process for the treatment of scrap tyres: preliminary experimental results". In: *Waste Management* 22.8 (2002), pp. 917–923.

[14] WM Grundy, B Schmitt, and E Quirico. "The temperature-dependent spectrum of methane ice I between 0.7 and 5 μm and opportunities for near-infrared remote thermometry". In: *Icarus* 155.2 (2002), pp. 486–496.

[15] D Hirsch and A Steinfeld. "Solar hydrogen production by thermal decomposition of natural gas using a vortex-flow reactor". In: *International Journal of Hydrogen Energy* (2004).

[16] Anders Holmen, Ola Olsvik, and OA Rokstad. "Pyrolysis of natural gas: chemistry and process concepts". In: *Fuel Processing Technology* 42.2-3 (1995), pp. 249–267.

[17] *Infrared Spectroscopy*. (Cited 17-03-2021). Aug. 15, 2020. URL: `https://chem.libretexts.org/@go/page/1847`.

[18] Jr. John D. Anderson. *COMPUTATIONAL FLUID DYNAMICS, The basics with Applications*. 1995.

[19] Punitkumar R Kapadia, Michael S Kallos, and Ian D Gates. "Potential for hydrogen generation from in situ combustion of Athabasca bitumen". In: *Fuel* 90.6 (2011), pp. 2254–2265.

[20] Ke Liu, Chunshan Song, and Velu Subramani. *Hydrogen and syngas production and purification technologies*. John Wiley & Sons, 2010.

[21] Warren Lee McCabe, Julian Cleveland Smith, and Peter Harriott. *Unit operations of chemical engineering*. Vol. 5. McGraw-hill New York, 1993.

[22] Ola Olsvik and Francis Billaud. "Thermal Coupling of Methane-A Comparison Between Kinetic-Model Data and Experimental-Data". In: *Thermochimica acta* 232.1 (1994), pp. 155–169.

[23] Nesrin Ozalp and Devanuri JayaKrishna. "CFD analysis on the influence of helical carving in a vortex flow solar reactor". In: *international journal of hydrogen energy* 35.12 (2010), pp. 6248–6260.

[24] Richard Langley Stephen F. Austin State Paul Flowers Klaus Theopold and William R. Robinson. *Chemistry*. 2015.

[25] Stephen A Rackley. *Carbon capture and storage*. Butterworth-Heinemann, 2017.

[26] Chris Riedy. "Climate Change". In: Aug. 2016. ISBN: 9781405124331.

[27] Sylvain Rodat, Stéphane Abanades, and Gilles Flamant. "Co-production of hydrogen and carbon black from solar thermal methane splitting in a tubular reactor prototype". In: *Solar energy* 85.4 (2011), pp. 645–652.

[28] Sylvain Rodat et al. "Hydrogen production from solar thermal dissociation of natural gas: development of a 10 kW solar chemical reactor prototype". In: *Solar energy* 83.9 (2009), pp. 1599–1610.

[29] Scott C Rowe et al. "Nowcasting, predictive control, and feedback control for temperature regulation in a novel hybrid solar-electric reactor for continuous solar-thermal chemical processing". In: *Solar Energy* 174 (2018), pp. 474–488.

[30] MP Ruiz et al. "Soot formation from C2H2 and C2H4 pyrolysis at different temperatures". In: *Journal of analytical and applied pyrolysis* 79.1-2 (2007), pp. 244–251.

[31] Bernhard Schrader. *Infrared and Raman spectroscopy: methods and applications*. 2008.

[32] *Solar Energy Data in Norway, IA*. (Cited 10-04-2021). Apr. 10, 2021. URL: https://www.solarenergylocal.com/states/iowa/norway/.

[33] *SSB*. (Cited 10-04-2021). Apr. 10, 2021. URL: https://www.ssb.no/energi-og-industri/statistikker/elektrisitet.

[34] *STAR-CCM+, STAR-CCM+ User guide*. (Cited:11-03-2021). URL: file:///C:/Program%20Files/CD-adapco/13.06.012-R8/STAR-CCM+13.06.012-R8/doc/en/online/index.html#page/STARCCMP%2FGUID-7DED1D9B-AAA1-48D4-93A0-62B176764E35%3Den%3D.html%23.

[35] *STAR-CCM+, STAR-CCM+ User guide*. (Cited:11-03-2021). URL: file:///C:/Program%20Files/CD-adapco/13.06.012-R8/STAR-CCM+13.06.012-R8/doc/en/online/index.html#page/connect%2Fsplash.html.

[36] *STAR-CCM+, STAR-CCM+ User guide*. (Cited:09-03-2021). URL: file:///C:/Program%20Files/CD-adapco/13.06.012-R8/STAR-CCM+13.06.012-R8/doc/en/online/index.html#page/STARCCMP%2FGUID-DF7340FC-15A4-448F-95B8-D3279D4FB74D%3Den%3D.html%23.

[37] *STAR-CCM+, STAR-CCM+ User guide*. (Cited:09-03-2021). URL: file:///C:/Program%20Files/CD-adapco/13.06.012-R8/STAR-CCM+13.06.012-R8/doc/

en/online/index.html#page/STARCCMP%2FGUID-3A7C1AA6-74F0-458C-BF8F-BA9BDF8B5789%3Den%3D.html%23.

[38] *STAR-CCM+, STAR-CCM+ User guide*. (Cited:17-03-2021). URL: file:///C:/Program%20Files/CD-adapco/13.06.012-R8/STAR-CCM+13.06.012-R8/doc/en/online/index.html#page/STARCCMP%2FGUID-D77AF2D3-5815-44E4-A591-599D56818669%3Den%3D.html%23.

[39] *State of the global climate 2020, IA*. (Cited 21-04-2021). 2020. URL: https://library.wmo.int/doc_num.php?explnum_id=10444.

[40] Bernard P Tissot and Dietrich H Welte. *Petroleum formation and occurrence*. 2013.

[41] Kenichi Watanabe, Murray Zelikoff, and Edward C Inn. *Absorption coefficients of several atmospheric gases*. Tech. rep. AIR FORCE CAMBRIDGE RESEARCH LABS HANSCOM AFB MA, 1953.